Journal of Materials Research and Technology 33 (2024) 5457–5481

Contents lists available at ScienceDirect

Journal of Materials Research and Technology

journal homepage: www.elsevier.com/locate/jmrt

A comprehensive study of the effect of scanning strategy on IN939 fabricated by powder bed fusion-laser beam

Merve Nur Doğu [a,b,c,*], Seren Ozer [d,e], Mustafa Alp Yalçın [f], Kemal Davut [g], Muhannad Ahmed Obeidi [a,b], Caner Simsir [e], Hengfeng Gu [h], Chong Teng [h], Dermot Brabazon [a,b,c]

[a] I-Form, the SFI Research Centre for Advanced Manufacturing, Dublin City University, Dublin, Ireland
[b] School of Mechanical & Manufacturing Engineering, Dublin City University, Dublin, Ireland
[c] Advanced Processing Technology Research Centre, Dublin City University, Dublin, Ireland
[d] Department of Metallurgical and Materials Engineering, Atılım University, Ankara, Turkey
[e] Department of Metallurgical and Materials Engineering, Middle East Technical University, Ankara, Turkey
[f] Metal Forming Center of Excellence, Atılım University, Ankara, Turkey
[g] Department of Materials Science and Engineering, Izmir Institute of Technology, 35430, Urla, Izmir, Turkey
[h] Ansys Inc., 6975 Union Park Avenue, Suite 663, Cottonwood Heights, UT, 84047, USA

ARTICLE INFO

Handling editor: SN Monteiro

Keywords:
Powder bed fusion-laser beam (PBF-LB)
IN939
Electron backscatter diffraction (EBSD)
Microstructure
Scanning strategy
Residual stress

ABSTRACT

This study provides a comprehensive investigation into the effects of different scanning strategies on the material properties of IN939 fabricated using the PBF-LB process. The scanning strategies examined included alternating bi-directional scanning with rotation angles of 0°, 45°, 67°, and 90° between adjacent layers (named as shown), as well as alternating chessboard scanning with rotation angles of 67° and 90° (named as Q67° and Q90°). The results revealed that the 45° and 67° samples had the highest relative density, while the 0° and Q67° samples showed the highest average porosity. Moreover, various types of cracks, including solidification, solid-state, and oxide-induced cracks, were observed. Among the bi-directional scan samples, the 0° sample displayed the most extensive cracking and the highest σ_{max} residual stress values in both XZ and XY planes. Conversely, the 45° and 67° samples exhibited fewer cracks. Notably, the lowest σ_{max} residual stress in the XZ planes among the bi-directional scan samples was observed in the 67° sample. Additionally, microstructural analyses indicated differences in grain size and morphology, among the samples. Texture analysis indicated that the 0° and 90° samples exhibited strong cube textures, whereas the texture intensity weakened for the 45° and 67° samples. Moreover, the alternating chessboard scanning strategy led to rougher surfaces (higher Sa and Sz values) compared to the alternating bi-directional scanning strategy, regardless of the rotation angles. Furthermore, the microhardness values among the samples showed minimal variance, ranging between 321 ± 14 HV and 356± 7 HV.

1. Introduction

Metal additive manufacturing (AM) provides significant advantages over traditional manufacturing techniques. These include the production of metal parts with intricate geometric complexity in a single step, the ability to achieve design freedom through near-net-shape production, as well as reductions in material waste and tooling costs [1,2]. Among the metal AM processes, the powder bed fusion-laser beam (PBF-LB) process stands out as one of the most widely utilized processes. It has gained significant attention from both industry and academia due to the aforementioned advantages [3,4]. Typically, the PBF-LB process begins by spreading a layer of metal powder onto a build plate. Then, a laser beam selectively melts the desired area within the powder layer based on the 3D computer-aided design (CAD) file. This layer-by-layer process continues until the part is fully fabricated [5,6].

Nevertheless, despite its advantages, the PBF-LB process may still exhibit some inevitable defects when the combined effect of improper scanning parameters and inadequate powder melting occurs. This can

* Corresponding author. I-Form, the SFI Research Centre for Advanced Manufacturing, Dublin City University, Dublin, Ireland.
E-mail address: mervenur.dogu@dcu.ie (M.N. Doğu).

https://doi.org/10.1016/j.jmrt.2024.10.171
Received 10 May 2024; Received in revised form 7 October 2024; Accepted 17 October 2024
Available online 18 October 2024
2238-7854/© 2024 The Authors. Published by Elsevier B.V. This is an open access article under the CC BY-NC-ND license (http://creativecommons.org/licenses/by-nc-nd/4.0/).

lead to various issues that compromise the mechanical properties and hinder large-scale industrial commercialization. These issues include partially melted powder, undesired microstructures, poor surface finish, porosity, balling, surface and internal cracks, and poor bonding between layers, all of which are primarily associated with an unstable melt pool status [7,8]. Moreover, the inherent characteristics of the PBF-LB process, such as rapid solidification, high cooling rates (10^5–10^7 K/s), and repeated thermal cycles, result in non-equilibrium solidification, leading to significant residual stress [9,10].

In the PBF-LB process, there are over 100 processing parameters to consider [11]. The laser power, layer thickness, laser scanning speed, and hatch distance (the distance between successive laser passes) are the most studied parameters. By adjusting these parameters, the printing process can be optimized to achieve the desired material properties [11]. Moreover, the scanning strategy, involving various factors such as scanning directions, scanning sequence, scanning vector length, scanning vector rotation angle, scanning time, and hatch distance, plays a crucial role in determining the thermal history and the arrangement of melt tracks within the fabricated parts. Thus, it enables precise control over the microstructure and overall performance of the fabricated parts [6,12,13]. The most utilized scanning strategies in the PBF-LB process include uni-directional, bi-directional (zigzag), stripe, and chessboard/checkboard/island scanning strategies. In the uni-directional scanning strategy, the energy beam moves in the same direction throughout the process, resulting in long scanning vectors. In the bi-directional scanning strategy, adjacent parallel scanning vectors move in opposite directions, still with long scanning vectors. On the other hand, the chessboard/checkboard/island scanning strategy divides the area into small square cells, reducing the scan vector length. This strategy is achieved by alternately scanning adjacent cells, resembling the pattern of a chessboard or checkered board [13,14].

Jia et al. [13] conducted a comprehensive review of the effects of the scanning strategy in the PBF-LB process on the microstructure, surface roughness, density, mechanical properties, and residual stress. In large parts, a shorter scan vector length is generally advantageous for reducing residual stress and enhancing the mechanical properties of the fabricated parts. Strategies such as island or bi-directional scanning can effectively mitigate residual stresses and minimize distortion by controlling local temperature gradients and thermal cycles during the build process. Additionally, implementing a re-melting strategy can be beneficial for achieving enhanced densification, minimizing surface roughness and defects, improving mechanical properties, and reducing residual stresses [13,15–18]. Overall, the choice of scanning strategy in the PBF-LB process significantly impacts the material properties. Understanding these effects is significant for optimizing the process parameters and achieving desired material properties for specific applications.

The effect of scanning strategies on the material properties of Ni-base superalloys fabricated by the PBF-LB process such as IN625 [17,19,20], IN718 [12,15,16,18,21–24], Hastelloy X [22,25,26], CM247LC [27], and IN738 [28] has recently gained more attention. Wan et al. [24] investigated the grain structure and crystallographic texture of IN718 fabricated by the PBF-LB process. They found that applying a bi-directional strategy with 90° rotation scanning led to a pronounced competitive grain growth mechanism and a strong cube texture in the fabricated parts. Furthermore, Xu et al. [28] investigated the grain refinement and crack inhibition of IN738 by altering the scanning strategy (rotation of 0°, 67°, and 90° between layers, respectively) during the PBF-LB process. They reported that rotating the scanning direction by 67° during the PBF-LB fabrication of IN738, resulted in nearly crack-free microstructures featuring both local equiaxed and columnar grains. This approach led to an excellent balance of strength and ductility, highlighting the potential for grain refinement and enhanced crack suppression in this hard-to-weld superalloy through modifications in the scanning strategy, without altering the alloy composition.

IN939 is a precipitation-hardenable Ni-base superalloy, strengthened mainly by the formation of the L12-ordered γ' phase ($Ni_3(Al, Ti)$). It was developed in the late 1960s as a cast alloy to fulfill the need for a robust, highly corrosion-resistant alloy capable of prolonged operation at temperatures up to 850 °C. Its superior properties include microstructural stability at elevated temperatures, high-temperature corrosion, oxidation and creep resistance. It has been widely used for land-based (blades and vanes) and marine gas turbines, fuel nozzles, diffusers, turbine airfoils and aircraft engines [1,29]. The weldability of superalloys is often assessed based on the total concentration of Al and Ti elements, as they influence the volume fraction of the γ' phase. When the combined concentration of Al and Ti exceeds 6 wt.%, the risk of crack formation increases [30]. IN939 is considered fairly weldable yet crack-susceptible. Liquation cracking, often attributed to factors such as the presence of low melting phases, γ' phase, the eutectic $\gamma-\gamma'$ phase, and MC carbides, has been reported in the Heat Affected Zone (HAZ) of cast IN939 during tungsten inert gas (TIG) welding processes [31,32]. Additionally, solidification cracking and solid-state cracking have been observed in IN939 fabricated by the PBF-LB [33–35]. Compared to welding, extremely higher thermal gradients in PBF-LB lead to rapid heating and cooling, resulting in significant residual stresses that can worsen cracking issues in IN939, particularly hot cracking.

Research on IN939 fabricated by the PBF-LB is notably limited compared to studies on other Ni-base superalloys [34,36–44]. Despite recent interest in IN939 fabricated by the PBF-LB, there is a significant lack of understanding regarding the impact of scanning strategies on its material properties. This study aims to address the existing gap in research by examining the effects of various scanning strategies on the material properties of IN939 fabricated by the PBF-LB. Specifically, the effects of different scanning strategies, including alternating bi-directional scanning with rotations of 0°, 45°, 67°, and 90° between adjacent layers, as well as alternating chessboard scanning with rotations of 67° and 90° between adjacent layers were investigated on the relative density, pore and crack formation, surface roughness, microstructure, crystallographic texture, microhardness, and residual stress of IN939 fabricated by the PBF-LB.

2. Materials and methods

2.1. Fabrication of IN939 samples by the PBF-LB process

In this study, gas atomized IN939 powder (Truform 939-N65, Praxair Surface Technologies) whose chemical composition is given in Table 1 was used to fabricate IN939 samples. Additionally, a comprehensive characterization of IN939 powder was reported in our previous study [1].

IN939 cubic samples (10 mm × 10 mm × 10 mm with 2 mm support), as shown in Fig. 1, were fabricated under a protective argon atmosphere (using 99.999% pure argon gas to maintain oxygen levels below 100 ppm). The samples were fabricated using an Aconity MINI (GmbH) metal 3D printer, equipped with an IPG YLR-200-WC-Y11 ytterbium fiber laser from the 2011 series.

Process parameters used for the fabrication of the samples, along with details of the samples are given in Table 2. During the processing, a supply factor of 3 was used to provide enough powder to build area for each layer. In addition, the volumetric energy density, VED (J/mm^3) was calculated as 62.5 J/mm^3 by taking the laser power, P (W), laser speed, υ (mm/s), layer thickness, t (mm) and hatch spacing, h (mm). The same formula was used in our previous study to calculate VED [29].

Fig. 1 shows six different scanning strategies used to fabricate IN939 samples in this study, along with the build plate pictures after fabrication. In addition to Fig. 1, Video-1A of Appendix A and Table 2 also give the details about the scanning strategies used to fabricate IN939 samples. Netfabb software (a product of Autodesk) was used to prepare files for fabrication. Scanning strategy in the software includes the combination of the scanning pattern (or hatching type), hatch starting angle

Table 1
The chemical composition (wt.%) of the gas atomized IN939 powder.

Elements	Al	Co	Cr	Nb	Ta	Ti	W	Zr	Ni	B	C	O	N
wt.%	1.9	18.9	22.8	1.0	1.4	3.8	2.0	0.028	Bal.	0.004	0.16	0.014	0.009

Table 2
PBF-LB process parameters utilized in the present study.

Laser power (W)	Laser scan speed (mm/s)	Layer thickness (mm)	Hatch spacing (mm)	Off-set (contour) (mm)	Spot size (mm)	VED (J/mm^3)
200	1000	0.04	0.08	0.05	0.08	62.5
Sample	**Scanning strategy**					
0°	Alternating bi-directional scan with no rotation between the adjacent layers					
45°	Alternating bi-directional scan with 45° rotation between the adjacent layers					
67°	Alternating bi-directional scan with 67° rotation between the adjacent layers					
90°	Alternating bi-directional scan with 90° rotation between the adjacent layers					
Q67°	Alternating chessboard scan with 67° rotation between the adjacent layers					
Q90°	Alternating chessboard scan with 90° rotation between the adjacent layers					

and position, hatch rotating angle per build layer, off-set (contour), and up and down skin [6]. As Table 2 displays, the first four scanning strategies were called alternating bi-directional scan (also called simple scan in Netfabb software) and the only difference between them is the rotation angle (0°, 45°, 67° and 90°) between the adjacent layers shown in Fig. 1(a–d). The last two scanning strategies were called alternating chessboard scan (also called quad scan in Netfabb software) with two different rotation angles (67° and 90°) exhibited in Fig. 1(e and f). In the chessboard scanning strategy, each layer was divided into small islands (island size 2.5 mm × 2.5 mm) forming a chessboard pattern and the overlapping gap was 0 mm.

Supplementary video related to this article can be found at https://doi.org/10.1016/j.jmrt.2024.10.171

2.2. Surface roughness measurements

The surface roughness measurements of the as-built samples were characterized with Bruker ContourGT from three samples for each scanning strategy to obtain the average values of the samples (over an area of 2 mm × 2 mm on the XZ planes of the samples). Sa value, which expresses the height of each point compared to the arithmetical mean plane, was used to describe the surface roughness directly. Also, the Sz value, which represents the sum of the maximum peak height and the maximum pit depth, was calculated.

2.3. Microstructural characterization

For the metallographic examination, IN939 cubic samples were sectioned by a precision cutter (Buehler IsoMet 5000) to investigate both observation directions shown in Fig. 1(g) (XZ plane which is parallel to the build direction (BD) and XY plane which is perpendicular to the BD). Before the analyses, the as-built samples were hot mounted with conductive Bakelite and were automatically ground using conventional SiC grinding papers (320, 500, and 800 grit sizes) and polished with progressively finer diamond suspensions (9, 3, and 1 μm). An additional final polishing step using 0.25 μm fumed silica (OP–S) was applied for electron backscatter diffraction (EBSD) analysis. Then, as-polished samples were etched with the Glyceregia reagent (15 ml HCl, 10 ml glycerol and 5 ml HNO_3) for further microstructural examination.

Keyence VHX2000E optical 3D digital microscope (OM) and Carl Zeiss Merlin Field Emission Gun Scanning Electron Microscope (FEG-SEM) were used for microstructural examinations. Zeiss EVO LS 15 equipped with Oxford EDS detector was used for energy dispersive X-ray spectroscopy (EDS) analysis (an acceleration voltage of 15 kV, 3.0 nA probe current, WD: 8.5 mm).

EBSD analysis was carried out with the ZEISS Merlin SEM using 15 kV acceleration voltage, 6.0 nA probe current. EBSD maps of 325 μm × 325 μm were measured on a hexagonal grid with a step size of 0.75 μm. EBSD raw data was post-processed using TSL OIM Analysis v7.3.1 software and points having CI (confidence index) below 0.1 were removed from datasets. Additionally, texture analyses were performed using the generalized spherical harmonic series expansion method of Bunge [45]. The harmonic series were expanded to a rank (L) of 34, and a Gaussian smoothing with a half-width of 5° was used.

The phase contents of the samples were determined by X-ray diffraction (XRD) analysis with Bruker D8 Advance Eco device using Cu-Kα radiation at 40 kV via continuous scanning between 30° and 100° 2θ angles with a scan speed of 0.5°/min. All samples were ground using SiC papers before the XRD analysis.

2.4. Relative density and porosity measurements

The relative density of the as-built samples was measured by Archimedes' method from six samples for each scanning strategy to obtain the average relative density values of each scanning strategy with the help of Sartorius Entris II Essential BCE124I–1S analytical balance having an accuracy and repeatability of ±0.1 mg according to ASTM B311-17 [46]. Acetone (Honeywell, purity ≥99.80%, density at 20 °C: 0.79 g/cm^3) was used as the fluid. Measurements were repeated three times for each sample. Additionally, the theoretical density of fully dense IN939 was taken as 8.15 g/cm^3 to calculate the relative density values of the samples [47].

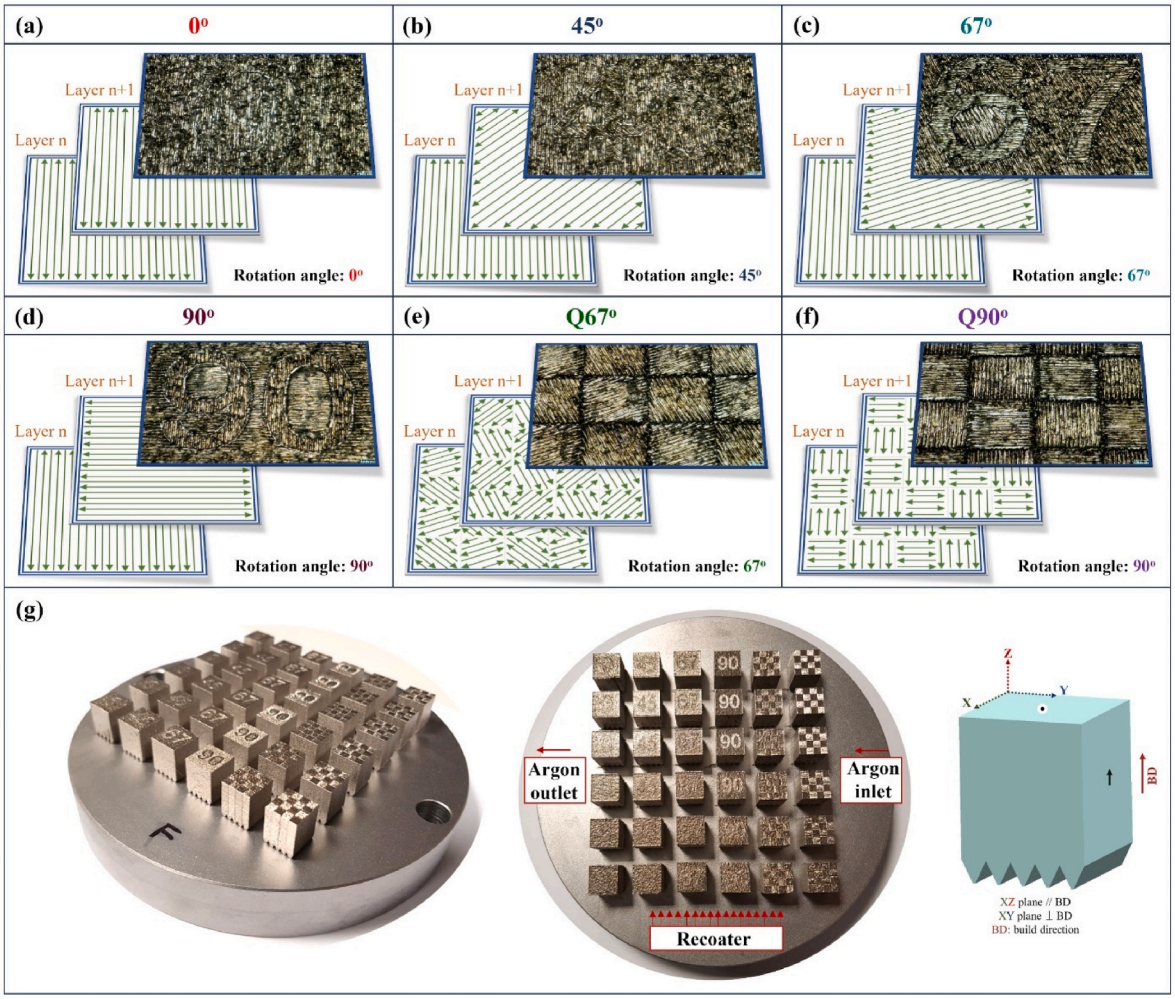

Fig. 1. Schematics of the scanning strategies: alternating bi-directional scan with (a) no rotation (b) 45° rotation, (c) 67° rotation, (d) 90° rotation between the adjacent layers, and alternating chessboard scan with (e) 67° rotation and (f) 90° rotation between the adjacent layers. (e) Pictures of the build plate after fabrication and schematic of the as-built samples.

Optical microscopy was used to analyze porosity distribution. The as-polished cross-section optical images (from both XZ and XY planes) were taken using the stitching property of the Keyence 3D optical microscope. For the porosity calculation, the stitched optical images including at least 20 images at 100X were analyzed using ImageJ software.

2.5. Microhardness and residual stress measurements

The Vickers microhardness values of the as-built samples were calculated from the average of 15 measurements for each XZ and XY plane of the samples using Zwick/Roell ZHV10 microhardness tester with a load of 1 kg and by the ASTM E384 standard [48].

The electropolishing process was conducted on the both XZ and XY planes of the as-built samples using Struers Movipol-5 equipment with specific parameters: 45 V, 20 s duration, and 20 flow rate. An A2 electrolyte solution, consisting of 90 ml distilled water, 730 ml ethanol, 100 ml butoxyethanol, and 78 ml perchloric acid, was utilized for layer removal and depth profile measurements [49]. Around 100 μm of material was removed from the surface of the samples with electropolishing, and the depth was measured using a Mitutoyo micrometer gauge.

XRD residual stress measurements were conducted using the Xstress_3000_G2R measurement device manufactured by Stresstech, with XTronic software version V1.14.0. This equipment and measurement strategy comply with the European X-ray residual stress testing standard EN 15305. Before the experiments, the system is aligned according to the ASTM E915 standard [50] and focal length is determined by using an interlaboratory certified IN625 powder and interlaboratory calibrated shot peened IN718. For measurements, manganese (Mn-Kα) radiation having a wavelength of 2.10314 Å was used as the X-ray source. A collimator with a 2 mm diameter was utilized, positioned at 10 mm from lower-left corner of all samples. The detector distance from the samples was 50 mm, with an arc radius of 50 mm. Exposure time was maintained at 10 s, and the number of tilts ranged from −8 to +8 (with a tilt angle of −45° to +45° and without oscillation). The Poisson's Ratio (ν) and Modulus of Elasticity (E) values used were 0.28 and 167 GPa, respectively. Stress values were then calculated at angles of 0°, 45°, and 90°, from those values principal stress (σ_{max} and σ_{min}) and the orientation of the maximum principal stress with respect to global axes ($\Phi(\sigma_{max})$) were determined under plane-stress assumption.

3. Results

3.1. Relative density and porosity

The relative density values are depicted in Fig. 2(a). The results indicate that the 45° sample exhibits the highest relative density at 99.29%, whereas the Q90° sample shows the lowest relative density at 99.05%. Furthermore, the 67° sample demonstrates a relative density value of 99.28%, which is nearly identical to that of the 45° sample. In

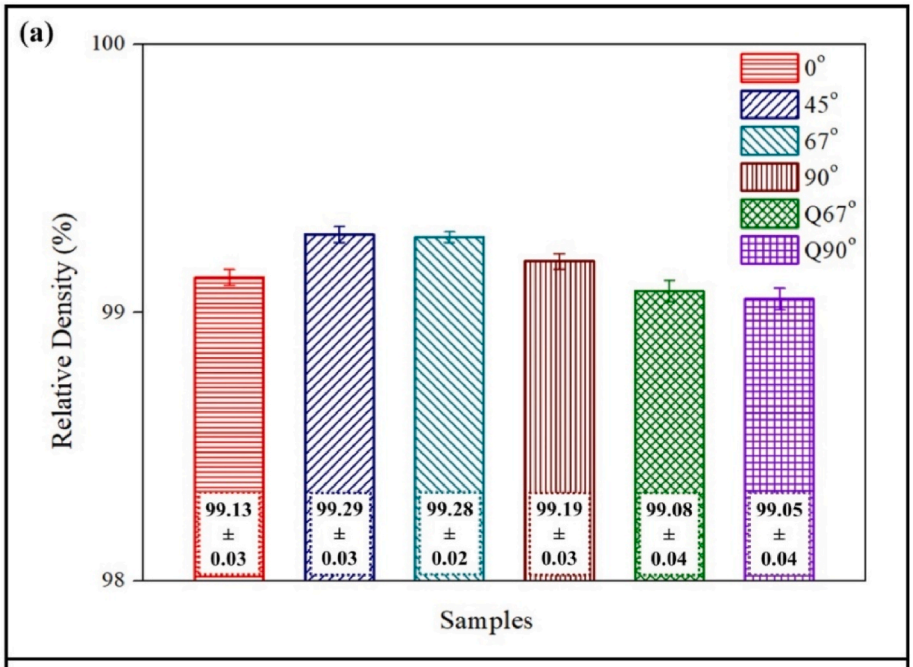

(b)

Sample	Porosity (%)	Pores/mm²	Average Feret Size (μm)
0°-XZ	0.39	17.74	20.47
0°-XY	0.14	10.14	22.04
0°-Average	0.27	13.94	21.26
45°-XZ	0.09	7.69	15.38
45°-XY	0.12	2.69	34.64
45°-Average	0.11	5.19	25.01
67°-XZ	0.08	5.77	13.47
67°-XY	0.05	3.92	16.57
67°-Average	0.07	4.85	15.02
90°-XZ	0.05	5.93	17.43
90°-XY	0.08	3.43	21.66
90°-Average	0.06	4.68	19.54
Q67°-XZ	0.07	1.67	23.31
Q67°-XY	0.47	13.02	19.52
Q67°-Average	0.27	7.35	21.41
Q90°-XZ	0.14	4.43	19.85
Q90°-XY	0.27	9.28	19.01
Q90°-Average	0.20	6.86	19.43

Fig. 2. (a) The relative density (error bars show 95% CI) and (b) ImageJ porosity analysis of the as-built samples obtained by different scanning strategies.

addition to the relative density values, Fig. 2(b) presents the results of the ImageJ porosity analysis for the XZ and XY planes of the samples, along with the average results, including porosity (%), pores/mm^2, and average Feret size (μm). According to the results, the 0° and Q67° samples exhibit the highest average porosity (%) at 0.27%, while the 90° samples show the lowest average porosity at 0.06%. Additionally, the average porosity (%) for the 67° sample is 0.07%, which closely resembles that of the 90° sample. The as-polished optical micrographs of the as-built samples in both XZ and XY planes are shown in Fig. 3. Among the alternating bi-directional scanning strategy, the highest defect formation such as pores and cracks were observed in the XZ plane of 0° sample (Fig. 3(a)) and this is supported by the pores/mm^2 value of 17.74. It should be noted that the pores/mm^2 value obtained from the ImageJ analysis of the PBF-LB fabricated samples provides insight into the porosity density within the material. A higher pores/mm^2 value indicates a higher concentration of pores, which can lead to decreased mechanical properties such as strength and fatigue resistance. Moreover, a lower pores/mm^2 value suggests a lower density of pores, which may indicate better material quality and integrity. Additionally, the typical size of pores in the sample can be interpreted from the average Feret size (a larger average Feret size suggests the presence of larger pores, whereas a smaller average Feret size indicates predominantly smaller pores). Therefore, controlling and minimizing the porosity, pores/mm^2, and average Feret size values are crucial for optimizing the

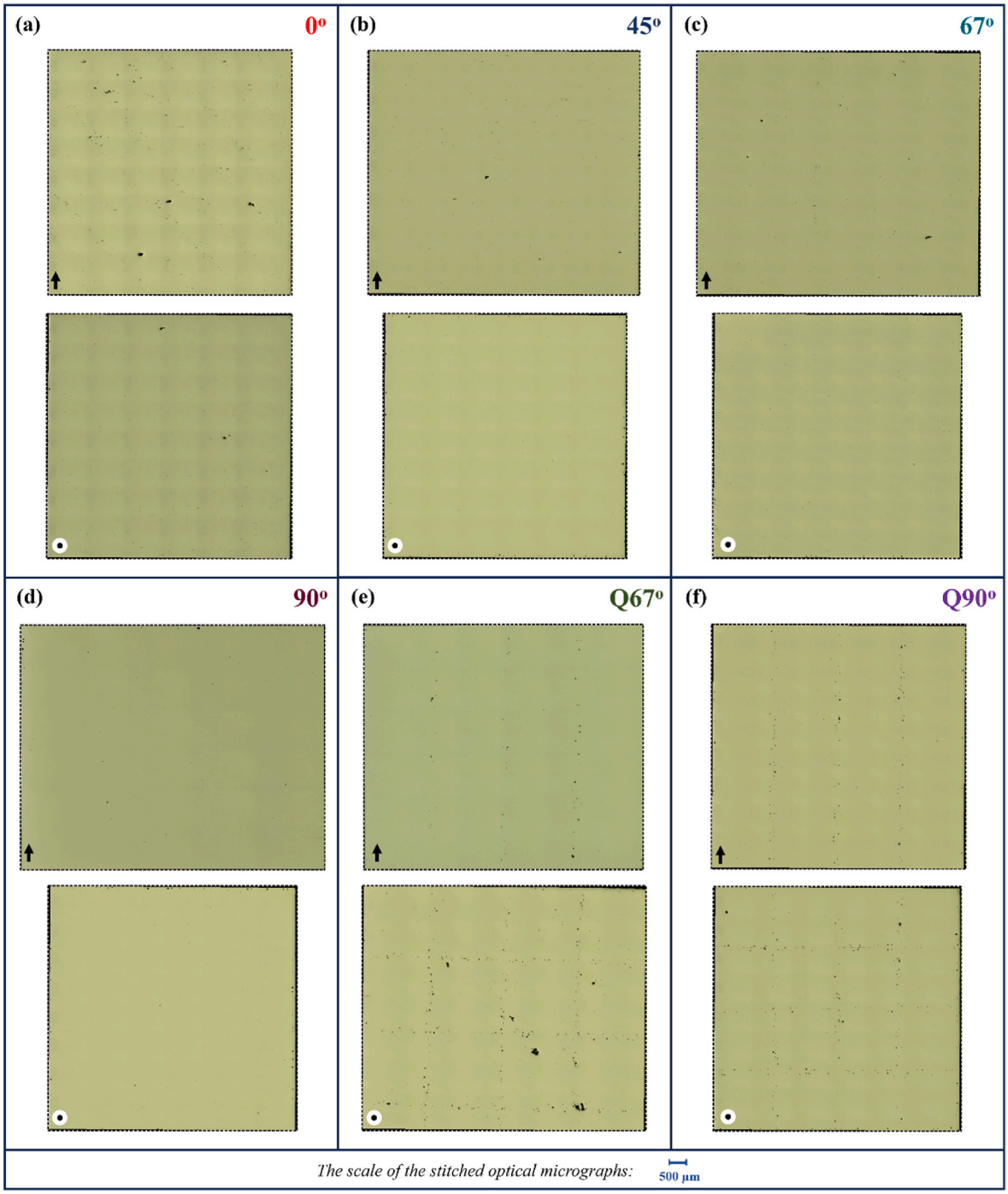

Fig. 3. The as-polished optical micrographs of as-built samples; (a) 0°, (b) 45°, (c) 67°, (d) 90°, (e) Q67°, and (f) Q90° in both XZ plane (parallel to the BD) and XY plane (perpendicular to the BD) are indicated with arrows and dots, respectively.

quality and performance of the PBF-LB fabricated components. Furthermore, a chessboard-like distribution of porosity was observed in the XY planes of the Q67° and Q90° samples. This pattern is likely attributed to a non-optimized overlapping ratio, as the overlapping gap was set to 0 mm in this study. Pores were also present in the overlapping regions of the XZ planes of the Q67° and Q90° samples. Moreover, pores/mm^2 is higher in the XY planes of these samples, whereas this is the opposite in the 67° and 90° samples. Among the six samples, the average Feret size is the lowest in the 67° sample, indicating that the smallest pores were formed when using the alternating bi-directional scan with a 67° rotation between adjacent layers.

3.2. Characterization of cracks

In the literature, the observed cracks for IN939 fabricated by the PBF-LB were categorized as solidification cracks and solid-state cracks [33]. Fig. 4 displays SEM images depicting the distribution of cracks observed in the XZ and XY planes of the as-built samples, with additional optical micrographs of these cracks provided in Fig. B1 of Appendix B. Among the samples, the 0° sample exhibits the highest degree of cracking. While most cracks propagate along the build direction (BD) in the XZ plane (especially near the edge of the sample shown in Fig. 4 (a2)), some cracks extend perpendicular to the BD (examples in Fig. 4 (a1, a3)). The cracks observed in the XZ plane of the 0° sample are notably long elongated through the BD, changing between about 5 and 450 μm in length. Consequently, these cracks traverse numerous deposition layers (40 μm layer thickness) along the BD.

The presence of a dendritic structure is characteristic of the solidification cracking, with cracks typically initiating between grains and propagating across the resolidified layers. This dendritic structure is evident in Fig. 4(a1, a5, b2, b3, c1, c3, d3, e3 and f2), indicating the presence of solidification cracks [33,51]. Additionally, some researchers suggest that initiation and propagation of solidification cracks perpendicular to the scanning direction are more probable due to the stress distribution along the laser path (an example in Fig. 4(a5)) [10,52]. On the other hand, the presence of Al and O in the same region, confirming the existence of aluminum oxide (Al_2O_3), was observed near some cracks as shown in Fig. 4(a3, a6). In addition to the 0° sample (Fig. 4(a2)), long cracks approximately 15–200 μm in length were observed near the edge of the 90° sample in the XZ plane, as shown in Fig. 4(d1). Tang et al. [33] reported similar kinds of cracks in IN939 fabricated by the PBF-LB, categorizing them as solid-state cracks. In contrast, the 45° and 67° samples exhibit fewer cracks in both the XZ and XY planes compared to the 0° and 90° samples. The cracks observed in the 45° and 67° samples are notably shorter in length, ranging approximately from 7 to 50 μm (Fig. 4(b and c)). Furthermore, cracks, pores and lack of fusion (LOF) defects, were particularly observed in and near the overlapping regions of the Q67° and Q90° samples.

Furthermore, the authors recommend that the examination of samples under SEM should be conducted after etching to check if the samples are crack-free. It was noted that while some microcracks were not visible after polishing, they became apparent after etching. This additional step ensures a more comprehensive assessment of crack formation.

3.3. Surface roughness

Fig. 5 displays the surface roughness profiles with average surface roughness (Sa) and the maximum height (Sz) values for the XZ planes of the as-built samples. Among the samples, the lowest Sa value (4.61 μm) belongs to the 90° sample, whereas the Q67° sample has the highest at 9.95 μm. Furthermore, the alternating bi-directional scan with a 67° rotation between adjacent layers results in the Sa value of 5.01 μm, whereas the alternating chessboard scan with a 67° rotation between adjacent layers yields the highest Sa value. Analysis of the surface roughness profile of the Q67° sample (Fig. 5(e)) reveals that the highest surface roughness is concentrated, particularly in the overlapping region. Additionally, the interior regions of the island in the Q67° sample exhibit random high surface roughness peaks. This is likely attributed to the increased spattering effect observed in this sample. Although the Sa value of the 0° sample (4.69 μm) is very similar to the 45° sample, there is a difference between Sz values (95.19 μm and 70.78 μm for the 0° and 45° samples, respectively).

3.4. Microstructure and crystallographic texture

The grain structure of the samples can be seen from the optical micrographs, SEM images (Fig. B2), the inverse pole figure (IPF) maps with respect to the BD, and image quality and grain boundaries (IQ and GBs) maps (Figs. 6–8). The Gaussian energy distribution of the laser beam in the PBF-LB process results in arc-shaped melt pools in the XZ planes, which are parallel to the build direction [1]. The arc-shaped melt pools, along with a microstructure composed of the columnar elongated grains along the build direction were observed in the XZ planes of the 45°, 67°, 90°, Q67°, and Q90° samples (Fig. B2 of Appendix B and Fig. 6). However, the XZ plane of the 0° samples did not show arc-shaped melt pools, whereas near directionally elongated columnar grains, and a few fine irregular grains were observed. On the other hand, the XY planes of the 67°, 90°, and Q90° samples (shown in Fig. 7) exhibited a distinct cross-like structure (chessboard pattern) attributed to the scanning rotation per layer [53]. Among them, the clearest chessboard pattern was observed in the XY plane of the 90° sample. Additionally, the Q67° sample displayed a slight chessboard pattern in the XY plane, whereas equiaxed grains were visible in the XY plane of the 45° sample. Moreover, the laser scan path was visible in the XY plane of the 0° sample, which did not show any chessboard pattern due to the absence of scanning rotation per layer. Furthermore, it can be said that all XY planes of the samples exhibited the equiaxed grains. In addition to this, Fig. 8 and Fig. B2 of Appendix B show the overlapping regions of the islands in the XY planes of the Q67° and Q90° samples. It can be especially seen from the IPF and IQ and GBs maps that the overlapping regions showed a mixture of equiaxed and columnar grains which are small and fine compared to the inside of the islands. Moreover, there was no significant difference between XRD patterns attributed to γ (gamma) phase of the as-built samples (Fig. B3 of Appendix B).

Grain major axis length, grain minor axis length, grain shape aspect ratio and grain shape orientation distribution graphs, and their values are exhibited in Fig. 9 and Table 3, respectively. In the 0° sample, the columnar grains were approximately twice as large as those in the other samples. Furthermore, the XZ planes of all the as-built samples possessed larger grains than the XY planes (Table 3). Additionally, the 45° and 67° samples exhibited smaller grains compared to the 90° sample, and the grains of the Q67° and Q90° samples were very similar to the 67° and 90° samples in terms of grain major and minor axis lengths. The grain major axis length distribution graphs (Fig. 9(a)) indicate a tri-modal distribution for the XZ plane of the 0° sample (peaks at around 100, 30, and 8 μm) and a bi-modal distribution for the rest of the samples (peaks at around 20 and 8 μm). On the other hand, bi-modal distribution was observed in the XY planes of all the samples, along with a higher peak at 20 μm and a minor peak at 10 μm for the 0°, 90°, Q67°, and Q90° samples. The grain minor axis lengths of the XZ planes are slightly larger than those of the XY planes, however, the differences among the samples are very low compared to the grain major axis length. The 90° sample exhibited the largest grain minor axis length among all as-built samples, with minor axis lengths in the XZ and XY planes being nearly identical. Nevertheless, the largest differences between XZ and XY planes were observed in the 45°, Q67°, and Q90° samples. It can be seen from Fig. 9 (b) that the grain minor axis length distribution graphs also exhibit bimodality (peaks at around 2 and 10 μm). In the 90° and Q90° samples, the peak at 10 μm was notably higher, whereas in the other samples, the peak at 2 μm was more pronounced.

The grain shape aspect ratio was notably smaller in the XZ plane of

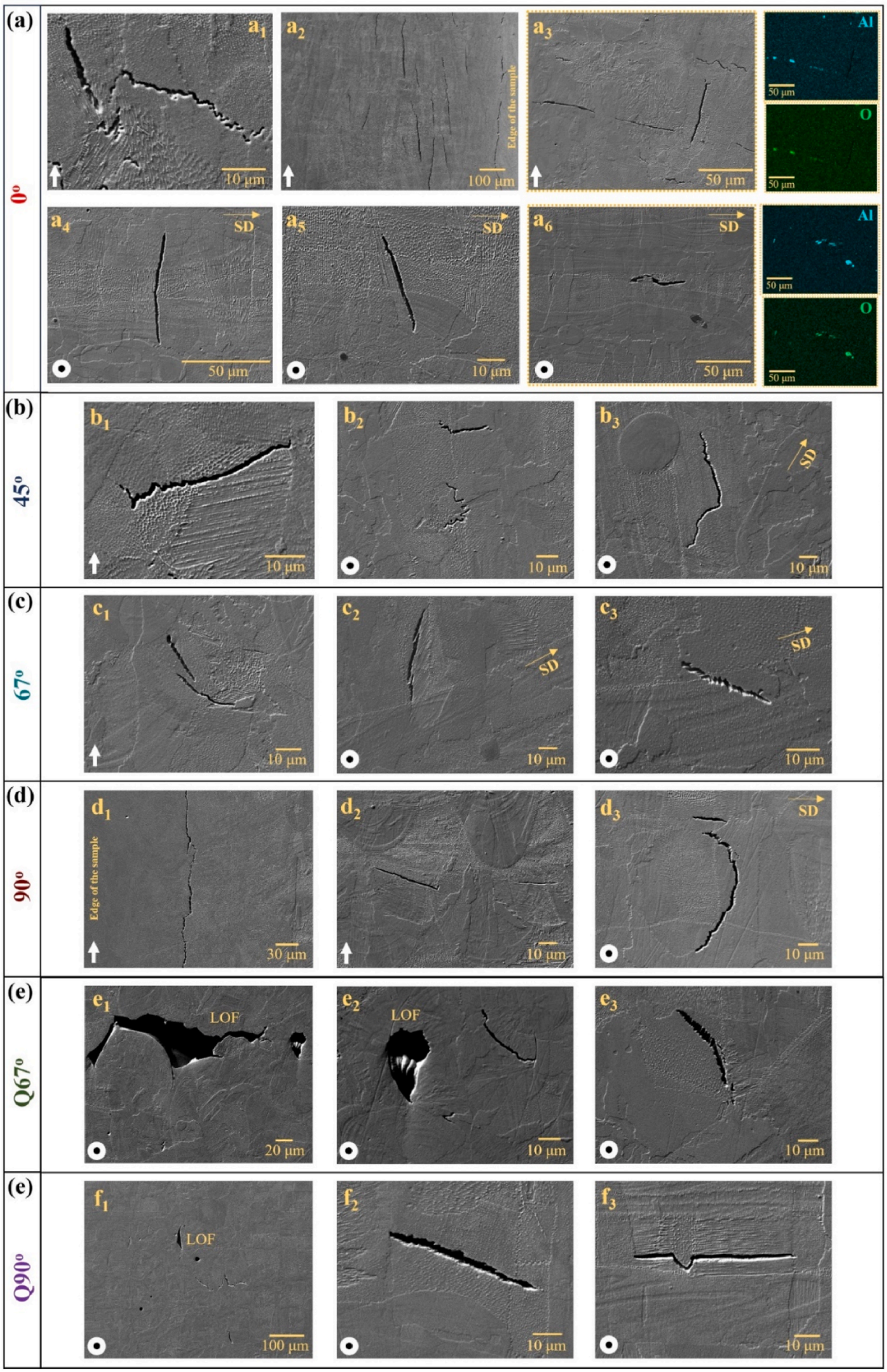

Fig. 4. SEM images of the crack distribution in the XZ and XY planes of the as-built samples: (a) 0°, (b) 45°, (c) 67°, (d) 90°, (e) Q67°, and (f) Q90°. (LOF: lack of fusion and SD: scanning direction).

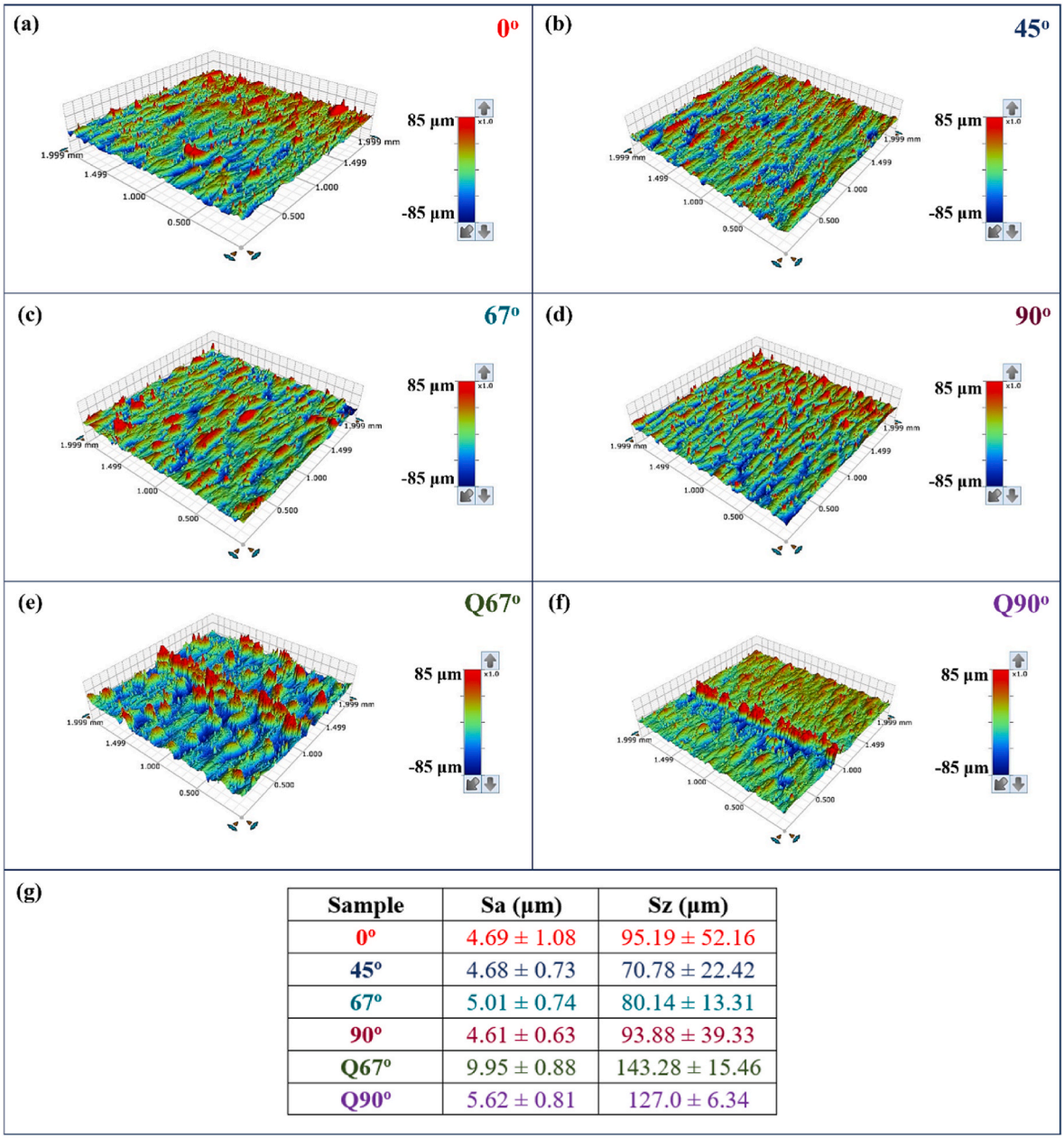

Sample	Sa (µm)	Sz (µm)
0°	4.69 ± 1.08	95.19 ± 52.16
45°	4.68 ± 0.73	70.78 ± 22.42
67°	5.01 ± 0.74	80.14 ± 13.31
90°	4.61 ± 0.63	93.88 ± 39.33
Q67°	9.95 ± 0.88	143.28 ± 15.46
Q90°	5.62 ± 0.81	127.0 ± 6.34

Fig. 5. The surface roughness profiles of the XZ planes of the (a) 0°, (b) 45°, (c) 67°, (d) 90°, (e) Q67°, and (f) Q90° samples, along with (g) Sa and Sz values.

the 0° sample compared to the other samples, indicating an exceptionally elongated grain structure (see Fig. 6(a) and B2 of Appendix B). Additionally, the grain aspect ratios for all samples were smaller in the XZ planes compared to the XY planes, primarily due to the presence of columnar grains. Also, note that the grain shape aspect ratio distribution graphs (Fig. 9(c)) show a minor peak around 0.8 aspect ratio (indicating an equiaxed grain structure); however, since those grains are smaller in size, their area fraction is less compared to more elongated grains. Moreover, the 90° and Q90° samples exhibited a narrower distribution of around 0.4 aspect ratio in the XZ plane, while the other samples displayed wider distributions for aspect ratio.

The grain shape orientation distribution graphs exhibited variations among samples and planes (Fig. 9(d)). The XZ plane of the 0° sample showed grains whose grain major axis is oriented vertically, which is parallel to the heat flow direction. Conversely, the remaining samples of the XZ planes displayed wider distributions, nevertheless having minor peaks around 45°, 67°,115°, and 135°. These peaks were also evident at similar angles in the XY plane. Here, grains in the samples were oriented such that their grain major axis is approximately 45° to the scan direction in the XY plane. For instance, in the XY plane, the 90° sample displayed a peak around 45°, whereas the 0° sample exhibits a peak at 135°.

The area-weighted average grain size, grain orientation spread (GOS), geometrically necessary dislocation (GND) density, and misorientation angle distribution graphs are given in Fig. 10. Also, Table 4 shows the area-weighted average grain size, GOS, kernel average misorientation (KAM), and GND density values. For all samples, the area-weighted average grain size values were larger in the XZ planes, showing a similar trend with the grain major axis length. In the XZ planes, the 0° sample exhibited the largest area-weighted average grain size of 23.7 µm, attributed to elongated columnar grains, while the 67° sample had the smallest size at 14.6 µm. Conversely, in the XY planes, the Q90° sample had the largest area-weighted average grain size of 13.9 µm, and the Q67° sample had the smallest at 9.7 µm. Moreover, the

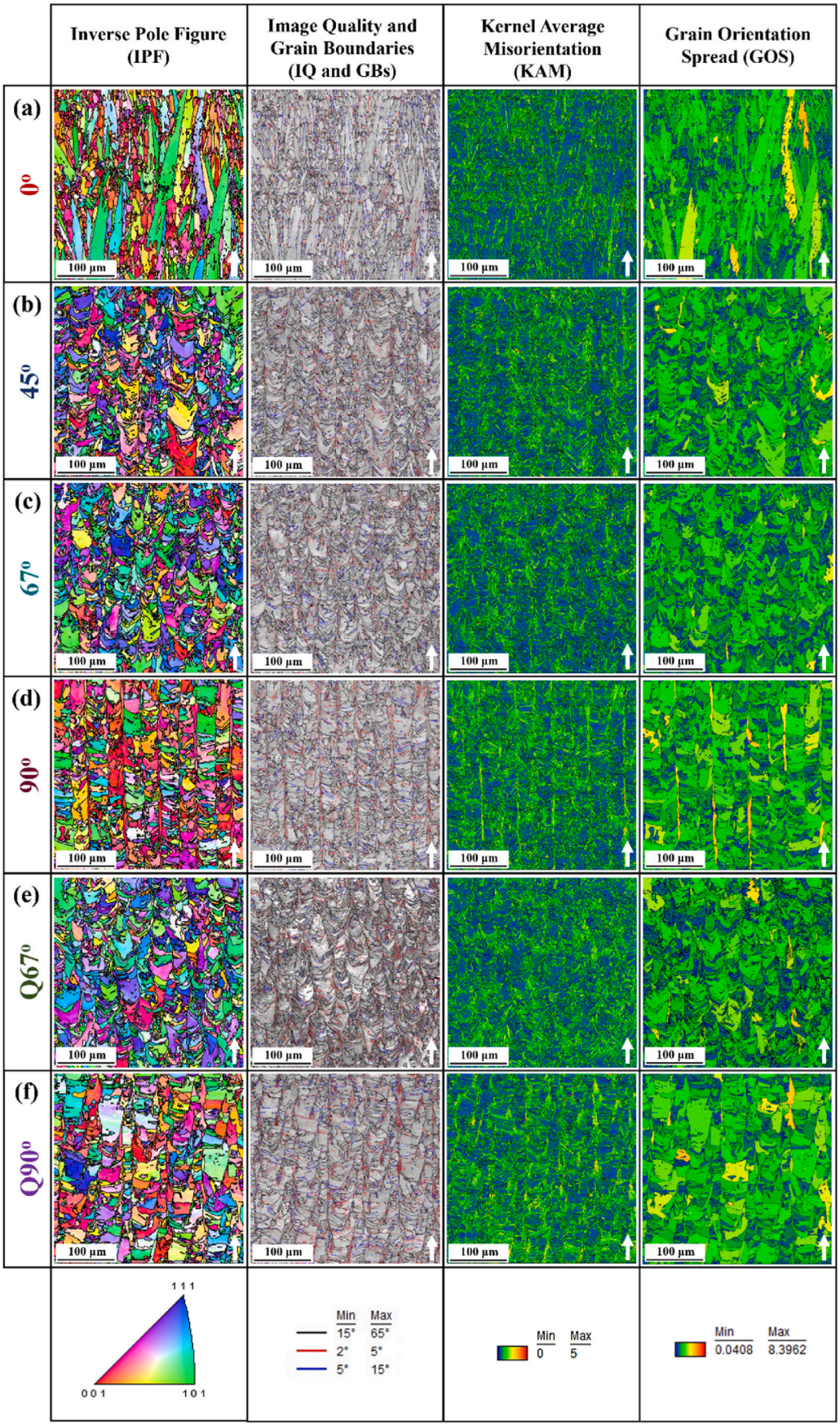

Fig. 6. EBSD maps of the XZ planes of the as-built samples: (a) 0°, (b) 45°, (c) 67°, (d) 90°, (e) Q67°, and (f) Q90°.

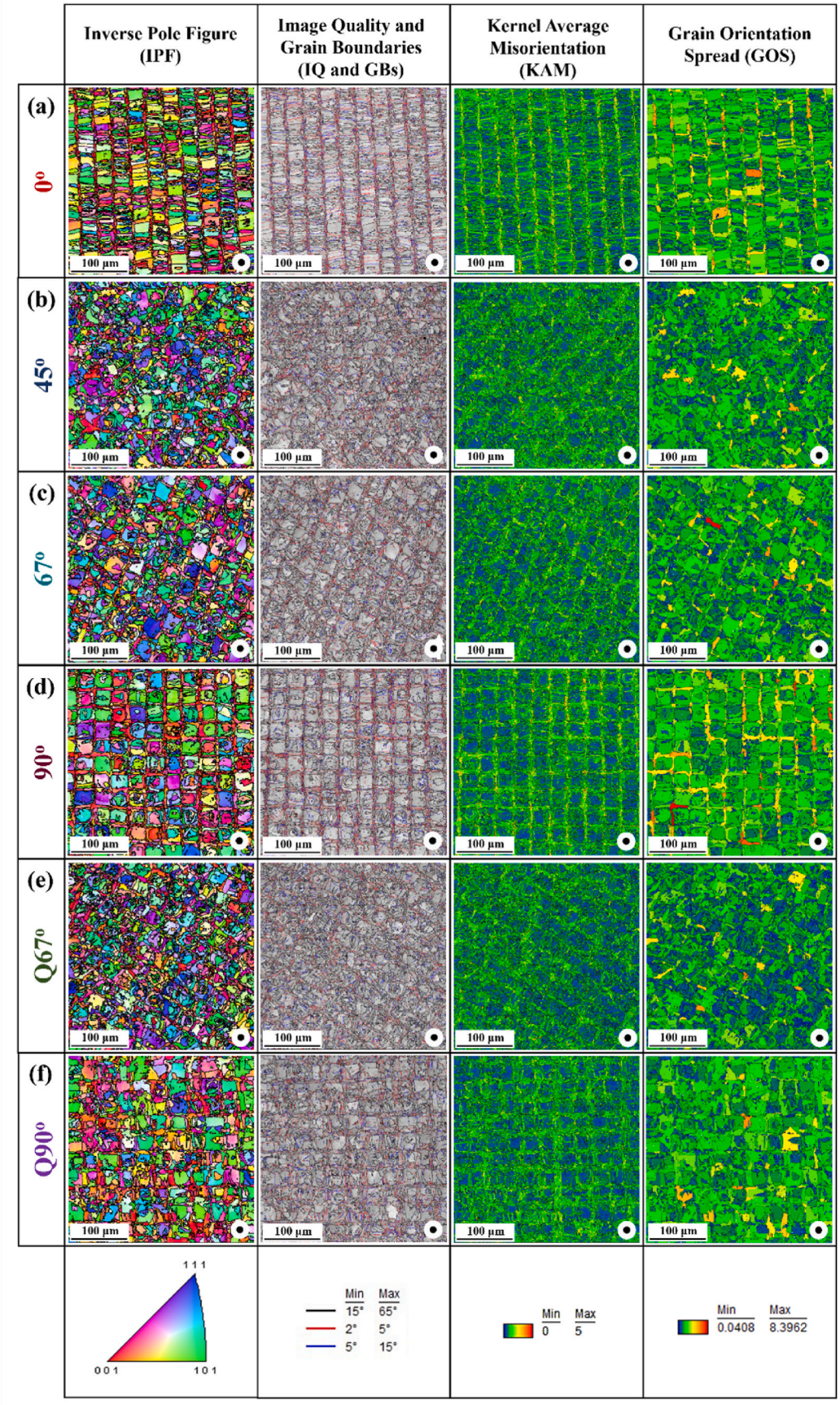

Fig. 7. EBSD maps of the XY planes of the as-built samples: (a) 0°, (b) 45°, (c) 67°, (d) 90°, (e) Q67°, and (f) Q90°.

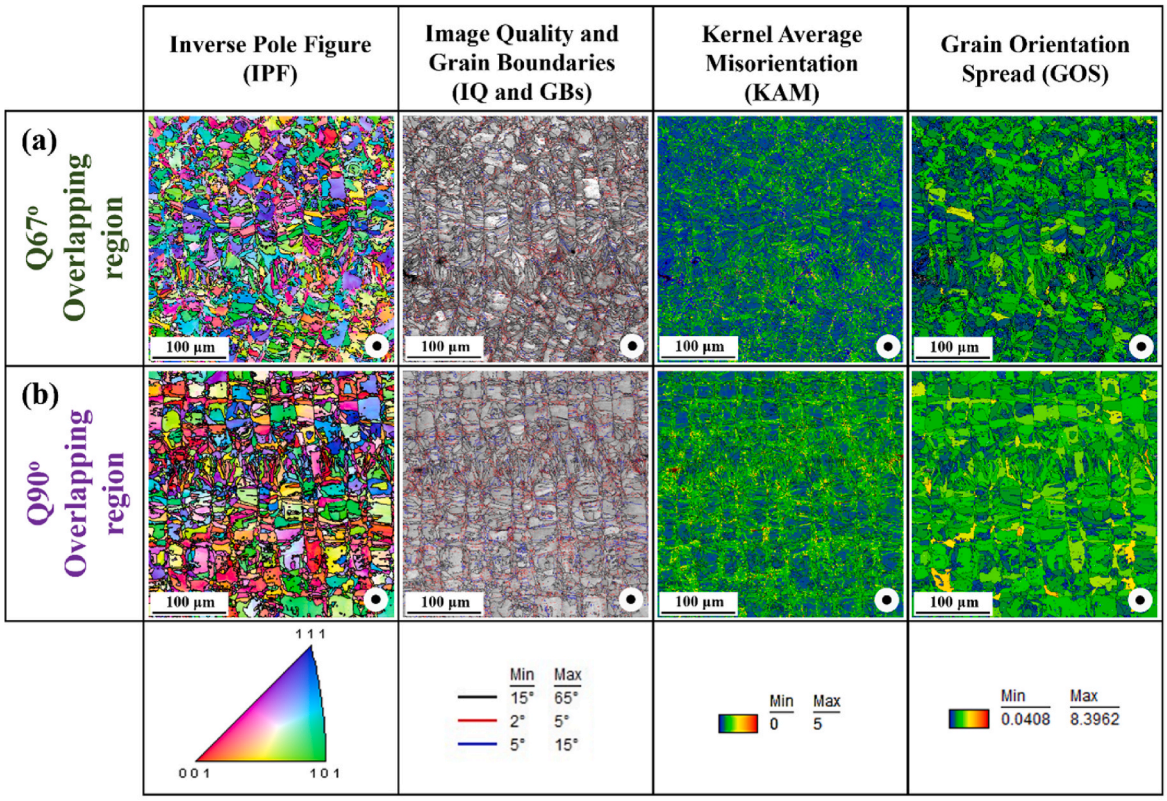

Fig. 8. EBSD maps of the overlapping regions of the as-built samples: (a) Q67° and (b) Q90°.

0° sample showed the largest anisotropy between the XZ and XY planes, with the XZ plane having the largest area-weighted average grain size (23.7 μm) and the XY plane having a smaller size (10.9 μm). In contrast, the 90° sample exhibited relatively consistent area-weighted average grain sizes in both the XZ and XY planes compared to other samples.

KAM is a measure of local misorientations and is closely associated with defect density. High KAM values are often attributed to high plastic strain and dislocation density within the material. It is calculated for each point in the EBSD map by determining the misorientations between a specific point and its surrounding points, followed by averaging these misorientations. Notably, misorientations exceeding 5° are excluded from the calculation of average misorientation, as they typically represent grain boundaries. The KAM maps (shown in Figs. 6–8) are color-coded using a rainbow scale, where blue and red represent the minimum misorientation and maximum misorientation (0°-5°). The chessboard pattern was prominently observed in the KAM maps of the XY planes for the 67°, 90°, and Q90° samples (Fig. 7). This pattern revealed regions with high lattice rotation and increased dislocation densities, corresponding to the centers of the melt pools. These areas indicated the presence of fine grains, as evidenced by the IPF, and IQ and GB maps [1,29]. Aota et al. [53] reported that the melt pool centerline has fine grains (at the borders of the chessboard pattern) and the overlapping regions of the melt pools (center of the chessboard pattern) have coarse grains. The XY planes of the samples had slightly higher KAM values than the XZ planes and there were minimal differences among the samples in terms of the KAM values (Table 4). The highest and lowest KAM values are 1.07° (in the XY plane of the 0° sample) and 0.86° (in the XZ plane of the 0° sample), respectively. Furthermore, in metallic materials, dislocation density includes both geometrically necessary dislocations (GNDs) and statistically stored dislocations (SSDs), and it is noted that GNDs constitute a significant portion of the total dislocations in face-centered cubic (FCC) metals. The rapid cooling rate during solidification induces local strain variations, leading to a higher dislocation density. GNDs arise from internal plastic strain gradients. Therefore, a high GND density is indicative of high plastic strain gradients [5,29]. The GND density values showed minimal variation like KAM values among the samples. The highest GND density was observed in the XY plane of the 45° sample (42.59×10^{12} m/m^3), while the lowest GND density was in the XY plane of the Q90° sample (34.14×10^{12} m/m^3). Additionally, there was variation between the XZ and XY planes in terms of KAM and GND values, similar to the area-weighted average grain size values, indicating anisotropy between the two planes.

GOS is a measure of local misorientation, focusing on grain-based local misorientation within the material. It is calculated by first determining the average orientation of a grain, followed by calculating the misorientation between this average orientation and the orientation of each individual measurement point within the grain. Subsequently, the average of these misorientations is calculated and assigned to each point within the grain. The rainbow scale is used for labelling the GOS maps like the KAM maps, where blue represents the minimum and red represents the maximum values (Figs. 6–8). High defect density and deformation lead to an increase in GOS values, while recrystallization tends to decrease them [1,29]. The XY plane of the 90° sample exhibited the highest GOS value at 2.23°, while the XY plane of the Q67° sample had the lowest GOS value at 1.63° among all the samples. GOS is also utilized to distinguish recrystallized grains from others. It is important to note that the choice of threshold GOS value for determining recrystallization fraction in EBSD analysis can vary depending on the material and analysis criteria. While there is no universally agreed-upon threshold value, a common threshold value used in some studies changes from 1° to 2.5° [28,29,53–56]. This threshold is chosen based on the assumption that grains with GOS values below this threshold have undergone recrystallization and are considered recrystallized grains, while grains with GOS values above this threshold are considered deformed grains. In this study, a threshold GOS value of $<1.5°$ was selected to calculate the recrystallization fraction, with GOS values

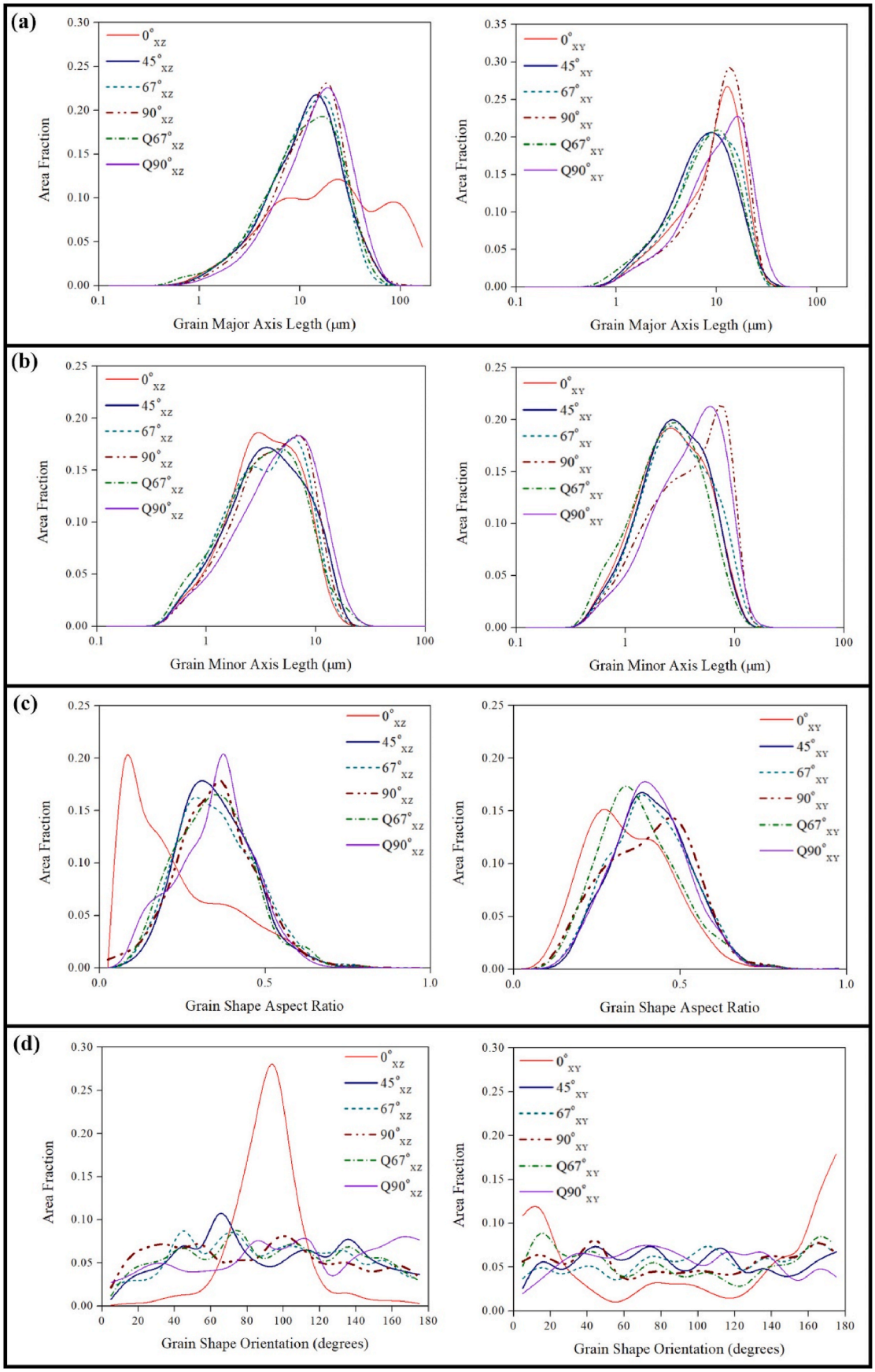

Fig. 9. (a) Grain major axis length, (b) grain minor axis length, (c) grain shape aspect ratio, and (d) grain shape orientation distribution graphs of the as-built samples for both the XZ and XY planes.

Table 3
Grain major axis length, grain minor axis length, grain shape aspect ratio, and grain shape orientation values of the as-built samples.

Sample	Grain Major Axis Length (μm)	Grain Minor Axis Length (μm)	Grain Shape Aspect Ratio	Grain Shape Orientation (degrees)
0°_{XZ}	36.37	4.23	0.23	91.52
0°_{XY}	9.90	3.22	0.34	99.21
45°_{XZ}	14.15	4.67	0.35	92.41
45°_{XY}	8.42	3.27	0.41	89.85
67°_{XZ}	13.09	4.36	0.35	91.15
67°_{XY}	8.92	3.56	0.40	97.48
90°_{XZ}	15.08	4.70	0.35	85.67
90°_{XY}	10.97	4.42	0.40	91.66
$Q67^{\circ}_{XZ}$	13.15	4.27	0.34	91.47
$Q67^{\circ}_{XY}$	8.44	2.92	0.37	88.17
$Q90^{\circ}_{XZ}$	16.95	5.62	0.35	100.90
$Q90^{\circ}_{XY}$	11.30	4.41	0.40	89.90

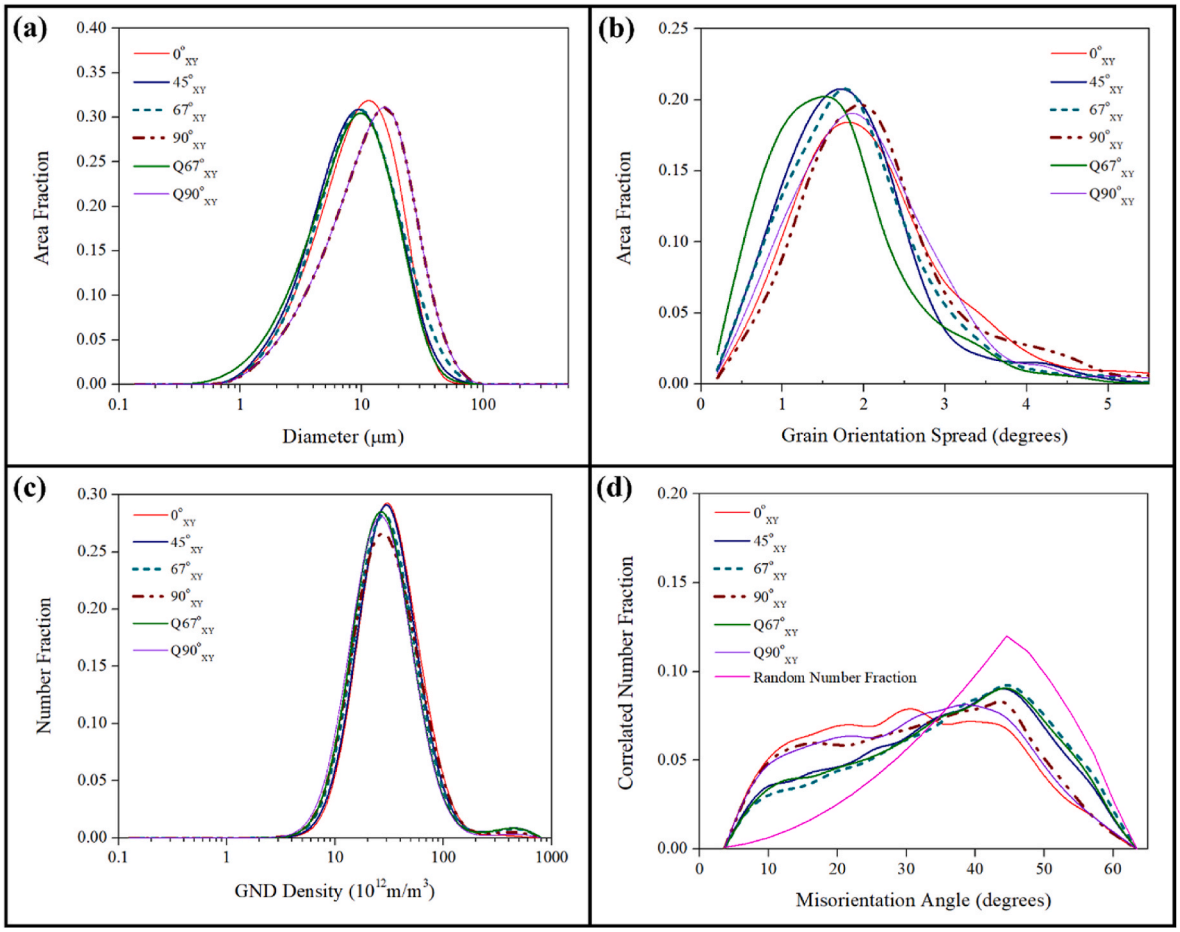

Fig. 10. (a) Area-weighted average grain size, (b) GOS, (c) GND density, and (d) misorientation angle distribution graphs of the as-built samples.

Table 4
Area-weighted average grain size, GOS, KAM, and GND density values of the as-built samples.

Sample	Average grain size (μm)	GOS (degrees)	KAM (degrees)	GND (10^{12} m/m^3)
0°_{XZ}	23.7 ± 21.3	2.03 ± 0.90	0.86 ± 0.47	34.36
0°_{XY}	10.9 ± 6.3	2.14 ± 1.03	1.07 ± 0.60	37.78
45°_{XZ}	15.7 ± 12.2	1.86 ± 0.77	0.87 ± 0.47	39.14
45°_{XY}	10.2 ± 6.3	1.82 ± 0.83	0.99 ± 0.52	42.59
67°_{XZ}	14.6 ± 9.7	1.74 ± 0.71	0.84 ± 0.45	38.50
67°_{XY}	11.0 ± 7.0	1.88 ± 0.91	0.97 ± 0.52	40.42
90°_{XZ}	16.2 ± 10.1	2.08 ± 0.90	0.93 ± 0.50	39.27
90°_{XY}	13.6 ± 7.8	2.23 ± 1.12	1.04 ± 0.59	38.90
$Q67^{\circ}_{XZ}$	15.5 ± 10.5	1.87 ± 0.79	0.87 ± 0.46	40.57
$Q67^{\circ}_{XY}$	9.7 ± 6.1	1.63 ± 0.85	0.93 ± 0.49	39.62
$Q90^{\circ}_{XZ}$	19.1 ± 13.2	2.15 ± 0.91	0.96 ± 0.54	37.81
$Q90^{\circ}_{XY}$	13.9 ± 8.0	2.01 ± 0.90	0.96 ± 0.52	34.14

below this threshold indicating recrystallized grains. The calculated recrystallization fractions of the samples are exhibited in Fig. 11 for both the XZ and XY planes. The highest recrystallization fraction was observed in the XY plane of the Q67° sample at 53.6%, while the lowest was in the XY plane of the 90° sample at 28.8%. Interestingly, in the XZ planes, the highest recrystallization fraction occurred in the 67° sample at 43.8%, and the lowest was in the Q90° sample at 31%. Furthermore, the detailed distribution of grain boundary characters of the samples extracted from IQ and GBs maps (shown in Figs. 6–8) is presented in Fig. B4 of Appendix B.

The misorientation angle distribution graph is displayed in Fig. 10(d) and the pink line represents the Mackenzie distribution for completely random-oriented cubic polycrystals. In the distributions of the as-built samples, a prevalence of low-angle grain boundaries (<15°) was observed, indicating the presence of more substructure regions and higher dislocation density. On the other hand, above 15°, which indicates high angle grain boundaries, misorientations approach to the Mackenzie. The 0° and 67° samples had the highest and lowest misorientations, respectively below 15°.

The corresponding {001}, {011}, and {111} pole figures (PFs) and inverse pole figures (IPFs) with respect to the build direction taken from the XY planes of the as-built samples are displayed in Fig. 12. Here, the intensity values are given in units of multiple random distribution (MRD), where an intensity value of 1 indicates a completely random distribution of crystallographic texture. The 0° and 90° samples exhibited a dominant cube texture having <100> parallel to scan and built directions. The intensity values of the PFs were 9.301 for the 0° sample and 6.930 for the 90° sample, while the intensity values of the IPFs were 3.999 for the 0° sample and 4.514 for the 90° sample. In addition to them, the Q67° sample also showed cubic texture (<100>// BD) with relatively lower intensity values of 2.250 for PFs and 1.675 for IPFs. Moreover, the 45°, 67° and Q90° samples displayed both <001>// BD and <101>//BD textures. Among them, the Q90° sample had higher intensity values (6.243 for PFs and 2.238 for IPFs) than the 45° and 67°

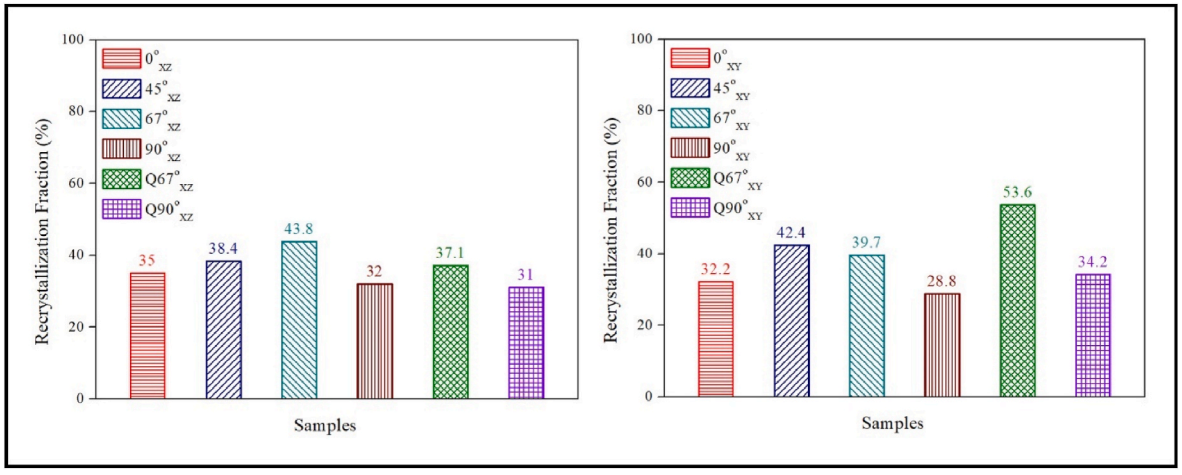

Fig. 11. Recrystallization fractions for both the XZ and XY planes of the as-built samples.

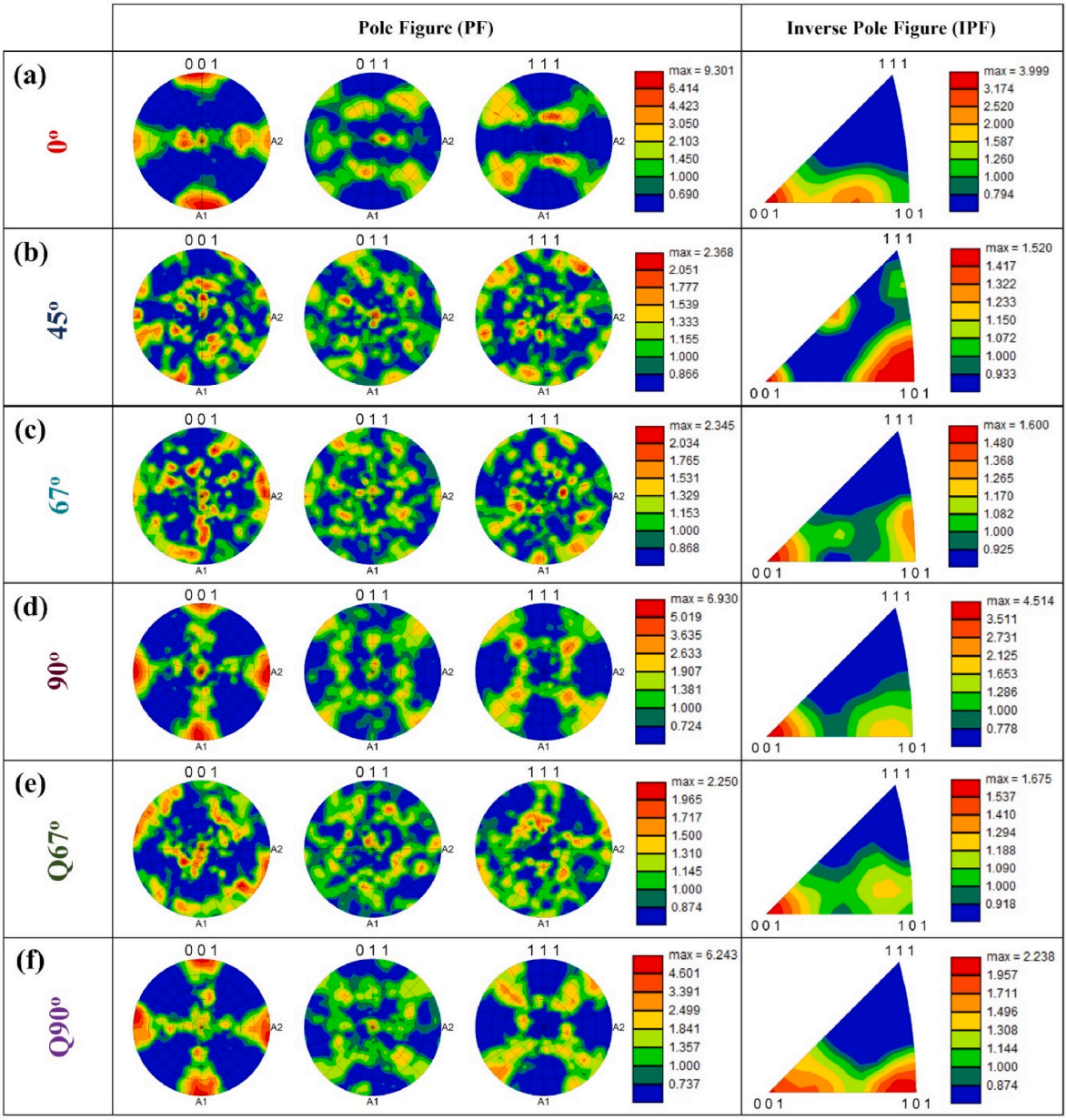

Fig. 12. Pole figures (PFs) and inverse pole figures (IPFs) with respect to the normal direction taken from the XY planes of the (a) 0°, (b) 45°, (c) 67°, (d) 90°, (e) Q67°, and (f) Q90° samples.

samples. Among all samples, the 0° sample had the most intense texture, whereas the 45°, 67°, and Q67° samples had low intensity values which are close to the random distribution of crystallographic texture.

3.5. Microhardness and residual stress

Fig. 13 shows the microhardness graphs of the as-built samples. There was a minimal variance in microhardness values among the samples. Within the XZ planes, the 0° sample displayed the highest microhardness value (356 ± 7 HV), whereas the Q90° sample exhibited the lowest (32 1± 14 HV). Conversely, the microhardness values in the XY planes were largely uniform across the samples. Notably, the microhardness graphs also highlighted anisotropy between the XZ and XY planes.

XRD residual stress measurements were conducted to determine the principal residual stresses (σ_{max} and σ_{min}) and the angle Φ (σ_{max}) (°) values, which are given in Fig. 14, according to the scanning strategy. The angle made by the X-axis and the maximum principal stress (σ_{max}) is denoted by Φ (phi). Moreover, Φ (σ_{max}) is the orientation of the maximum principal stress with respect to global axes. Among the XZ planes of the samples, the Q90° sample exhibited the highest σ_{max} residual stress (961.1 MPa), while the 67° sample showed the lowest (542.6 MPa). Additionally, the XZ plane of the Q67° sample displayed the lowest σ_{min} residual stress (129.3 MPa), whereas the Q90° sample demonstrated the highest (270 MPa). On the other hand, σ_{max} residual stress values of the XY planes of the as-built samples were close to each other. Among them, the Q67° sample had the lowest (408.4 MPa), whereas the 0° sample had the highest (581.6 MPa). Furthermore, the XY plane of the 67° sample possessed the lowest σ_{min} residual stress value (155.5 MPa), while the Q90° sample had the highest (493.9 MPa).

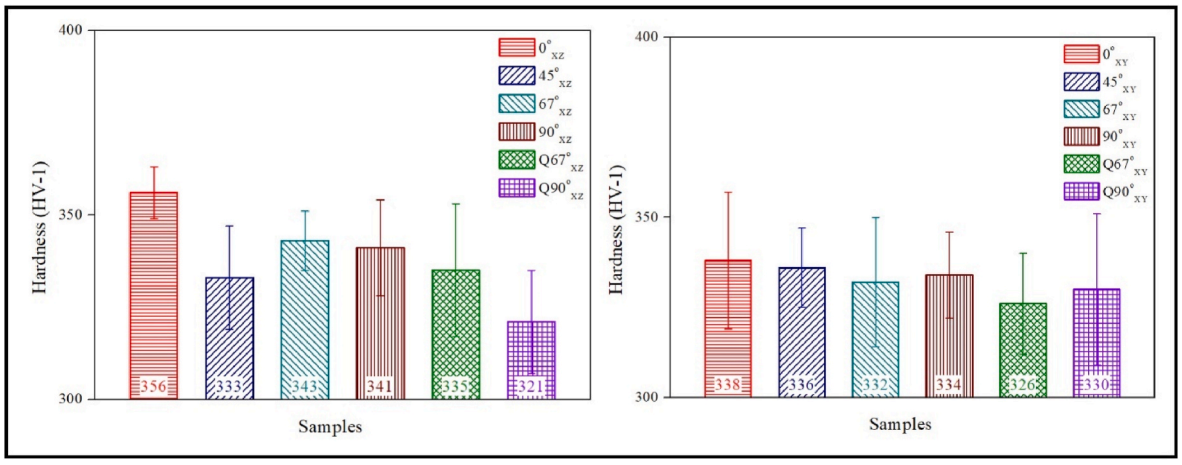

Fig. 13. Microhardness graphs for both the XZ and XY planes of the as-built samples.

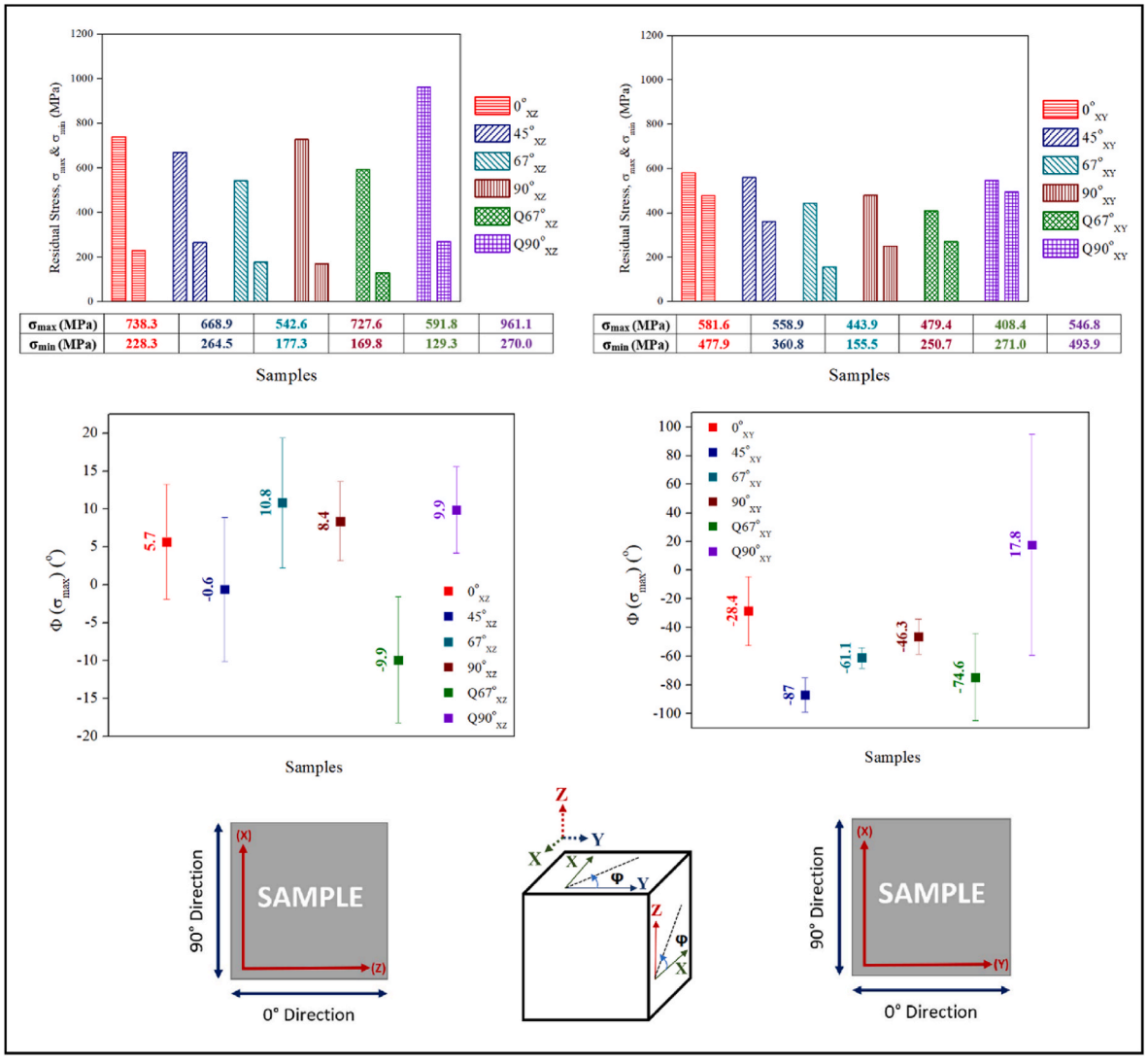

Fig. 14. The principal residual stresses (σ_{max} and σ_{min}) and Φ (σ_{max}) (°) graphs for both the XZ and XY planes of the as-built samples, along with a schematic representation of the Φ (°) corresponding to the observed planes.

4. Discussion

4.1. Relative density and defect analysis

Optimizing PBF-LB process parameters is significant for achieving desired outcomes, such as minimizing defects and reducing surface roughness. The scanning strategy plays an important role in tailoring material properties among these parameters, as evidenced by the current study [11,13]. The rotation between the adjacent layers increased the relative density of the samples, while reducing the pores/mm^2. This can be explained that layer-by-layer rotation promotes material fusion and fills voids between tracks, thus enhancing part density [12]. The lowest relative density observed in the chessboard scanning strategy, coupled with the presence of porosity and crack formation in the overlapping regions of small islands, can be attributed to the rapid opening, and closing of the laser. This rapid action introduces instability in laser energy input, potentially causing defects like pores and unmelted spatter powder at the boundaries of small islands [12]. Additionally, optimizing the overlapping gap, which was 0 mm in this study, between the islands for the chessboard scanning strategy can mitigate defects in the overlapping regions. Moreover, Lu et al. [57] reported that the island size significantly influences the formation of pores in IN718 fabricated by the PBF-LB. Smaller islands tend to result in the presence of unmelted and spatter powders in overlapping regions, leading to reduced density and increased porosity. According to their findings, as island size increased from 2×2 mm^2 to 7×7 mm^2, pore quantity, and size decreased notably with larger island sizes, indicating that denser parts can be achieved through the utilization of larger island scanning strategies [13,58]. In our study, using an island size of 2.5×2.5 mm^2 may have contributed to the observed low relative density, high porosity, and increased surface roughness. This is likely due to the greater presence of spattered powders associated with the smaller island size.

Superalloys rich in Al and Ti, such as IN939, are utilized to generate the L12-ordered γ' phase ($Ni_3(Al, Ti)$). However, these alloys are susceptible to cracking, presenting a significant challenge in the PBF-LB process for high γ' phase Ni-base superalloys [59]. The microcracking observed in IN939 produced by the PBF-LB process was reported in two primary types: solidification and solid-state cracks [33]. Solidification cracks, also known as “hot tears”, occur within the solidifying melt pool or mushy zone, where the material is in a semisolid state. The development of dendrite structures during solidification restricts the flow of residual liquid in the interdendritic regions, concentrating solidifying stress and potentially causing the tearing of liquid films and the formation of cracks. Furthermore, solid-state cracks can include various types, such as strain-age cracks, ductility-dip cracks (DDC), and cold cracks. These cracks can traverse both grains and grain boundaries, typically following a straight or slightly curved path within the grain structure, while also delineating and separating grains along their boundaries [51,59]. On the other hand, it has been reported that the presence of oxide can also contribute to crack formation through various mechanisms, such as stress concentration near the oxide, increased brittleness of boundaries, and constitutional liquation at the oxide-matrix interface [10,52]. In the current study, dendritic structures indicative of solidification cracks were observed within the cracks. Long and straight cracks, typically associated with solid-state cracks, were also noted. Additionally, Al_2O_3 was detected in some of the cracks, suggesting the presence of oxide-induced cracks.

Mukherjee et al. [60] highlighted the significance of grain structure in determining susceptibility to cracking. Specifically, the presence of long columnar grains can lead to their separation under high tensile stress during solidification, thereby contributing to the occurrence of solidification cracking. In our study, the XZ plane of the 0° sample, characterized by large columnar grains, exhibited the highest degree of cracking, aligning with this explanation. Moreover, fewer cracks were observed in the 45° and 67° samples compared to the 0° sample aligns with the study of Xu et al. [28] which highlights the critical role of scanning rotation angle in crack formation during the PBF-LB process. A 0° rotation accumulates strain in the same direction across layers, leading to high residual stresses and uneven temperature distribution, which promotes crack formation. In contrast, a 67° rotation angle distributes thermal stresses more evenly and reduces strain accumulation, resulting in fewer cracks. Similarly, a 45° rotation also improves stress distribution compared to 0°, but not as effectively as 67° as can be seen from the residual stress results in this study. While a 90° rotation can enhance long-term temperature uniformity, it may induce localized stresses due to abrupt changes in scanning direction, potentially increasing crack formation. The long and straight cracks observed near the edge of the 90° sample could be likely the result of these localized stresses. Overall, the 45° and 67° rotations offer better control over thermal gradients and stress distribution, minimizing the possibility of cracks.

4.2. Microstructural and crystallographic texture evolution

In the PBF-LB process, rapid cooling and non-equilibrium solidification influence the solidification microstructure, which is governed by parameters such as solidification rate (R), undercooling (ΔT), and temperature gradient (G). The size and morphology of the solidification microstructure (planar, cellular, equiaxed dendritic, or columnar dendritic) are determined by GxR and G/R, respectively [5,29,60,61]. Lower cooling rates result in coarser microstructures due to the lower product of the temperature gradient and solidification rate ($G \times R$), whereas higher cooling rates lead to finer microstructures. An extremely high G/R ratio results in planar solidification, while a moderate G/R ratio forms cellular structures, and a low G/R ratio generates columnar or equiaxed dendritic structures. In the PBF-LB process, typically high cooling rates lead to high G/R values, which favour cellular structures. Additionally, columnar dendritic structures can also occur. In this study, both columnar dendritic and cellular microstructures were observed (Fig. 4). Cellular structures, with a honeycomb-like morphology, appear as parallel boundaries along the build direction and as circular features on the transverse section, resulting in varied appearances in different cross-sections. This characteristic is widely observed in additively manufactured metals and alloys [44].

The findings of the current study revealed that altering the scanning strategy in the PBF-LB process has a substantial impact on the grain structure and texture of IN939. In the 0° sample, where the melt pools from successive layers are nearly aligned, a consistent temperature gradient is maintained between layers. This alignment results in a significant overlap of melt pools, effectively remelting portions of the previous layer and eliminating nucleation barriers. Consequently, the predominant heat flow direction aligns with the build direction, promoting epitaxial growth of columnar grains that extend along the build direction [12]. In the PBF-LB process, a laser forms a melt pool in the powder bed, melting new powder and partially remelting the previously solidified layer. This overlap creates a re-melting zone, influencing both the new and existing materials. Nucleation barriers, such as those from thermal gradients or existing grain structures, can impede the formation of new grains. However, high temperatures during remelting can dissolve these barriers, facilitating a more uniform material composition. This process enhances grain formation, leading to a more consistent microstructure with diverse grain orientations and sizes compared to areas where barriers persist. High nucleation barriers typically result in fewer, larger grains growing in a single orientation, creating an anisotropic microstructure. In contrast, low nucleation barriers allow for easier grain formation, promoting finer, more homogeneous, and isotropic microstructures. Moreover, the 45° and 67° samples have angled thermal gradients and varied melt pool orientations. This results in less uniform melt pool overlap and reduced removal of nucleation barriers, leading to more complex thermal conditions. These conditions can disrupt columnar grain growth, resulting in finer grains and reduced anisotropy. Research conducted by Liu et al. [12] and Song et al. [62]

indicates that rotating the scanning direction by 15° and 47° between layers can disturb columnar growth, hindering the epitaxial development of elongated grains and leading to more refined microstructures. Furthermore, the heat flow direction becomes perpendicular to the build direction in the 90° sample. This strategy enhances the uniformity of melt pool overlap and supports a competitive grain growth mechanism, thus promoting predominant epitaxial growth and potentially improving overall microstructural uniformity [12]. On the other hand, the chessboard scanning strategy promotes a uniform microstructure by preventing excessive heat buildup and ensuring consistent cooling rates, which refine grains in overlapping regions. This strategy disrupts the preferential growth of columnar grains, leading to finer grains. Steep temperature gradients in overlapping regions, caused by intersecting laser paths and varying thermal histories, significantly influence nucleation and growth dynamics, resulting in diverse grain orientations and sizes. The fine grains in the Q67° and Q90° samples' overlapping regions can be due to complex heat flow and faster cooling rates from intersecting laser points. The intermittent laser movement at island edges further accelerates cooling in these areas compared to island interiors.

In the PBF-LB process, recrystallization occurs due to thermal cycling during fabrication. High temperatures during melting and solidification cycles facilitate the creation of strain-free grains, replacing deformed ones [5,53–55,63]. Dynamic recrystallization (DRX), a subset of recrystallization, occurs in hot deformation processes like hot rolling or forging. It typically occurs above the recrystallization temperature of the materials, inducing the formation of new grains [64]. Recent research has shown that DRX can occur not only in traditional hot deformation processes but also in the PBF-LB process [28,65,66]. The expansion and contraction during the uniform rapid heating and cooling leads to a severe local plastic deformation that combined with the high cyclic temperatures and thermal stress in the PBF-LB process can be considered as a thermo-mechanical process. This process promotes the creation of new grains with lower dislocation densities, often resulting in a finer grain structure. Among the samples analyzed, the XZ plane of the 67° sample and the XY plane of the Q67° sample had the highest recrystallization fractions and the smallest area-weighted average grain sizes. These high recrystallization fractions indicate that the thermal cycles during these specific scanning strategies effectively dissolve existing nucleation barriers and facilitate the formation of new grains. This enhanced recrystallization leads to improved material homogeneity, potentially resulting in more consistent mechanical properties across the material.

The texture is determined by the combined effects of maximum heat flow directions and the alignment of easy grain growth directions at melt pool boundaries. In cubic crystal structures, the preferred grain growth direction is $< 100>$. This preference is due to the faster atomic movement along less densely-packed planes, which are more prevalent in this direction. These planes facilitate quicker and easier grain growth, making the $<100>$ direction energetically favourable for grain development. By locally altering the heat flow direction and the balance between G and R through adjustments in the PBF-LB process parameters like scanning strategy and energy density, the texture and microstructure can be modified [5,60,67]. Among the samples, the 0° and 90° samples exhibited a strong cube texture. In the 0° sample, the $<001>$ crystallographic direction aligns with laser trajectories in each layer. This uniform thermal flux across layers promotes epitaxial growth, favouring the $<001>$ crystal orientation due to reduced thermal gradients that encourage grain alignment along the easy growth direction. Moreover, in the 90° sample, achieving epitaxial growth of the $<100>$ texture requires grains to orient themselves at 15° to the maximum local heat flow direction. Perfect alignment with the heat flow direction results in a fiber texture, while misalignment leads to a cube texture. Additionally, an alternating bi-directional scanning strategy with 90° rotation between layers was found to strengthen the $<001>$ textures [24,61]. On the other hand, an alternating bi-directional scanning strategy with 45° and 67° rotations was found weaken the texture by producing finer microstructural features, as reported in previous studies [21,60,68,69]. This weakening was attributed to the reduction in the coincidence of laser scanning vectors between adjacent layers and minimized heat accumulation. The frequent changes in scanning direction and angle reduce thermal gradients, leading to more uniform temperature distribution across the build. Consequently, more nuclei participate in competitive growth, resulting in grain refinement and a more random grain orientation, which diminishes the strength of any preferred texture. Therefore, it can be said that the scanning strategy has a direct effect on the microstructure, recrystallization fraction, and grain size tailoring.

4.3. Residual stress evolution

Residual stress remains within the bulk of a material even in the absence of external loads. It typically arises from the accumulation of material hardening due to various factors such as phase transformations and temperature gradients during solidification and crystalline state changes. It is a common outcome of thermomechanical manufacturing processes, including AM, where layer-by-layer fabrication induces thermal expansion and contraction, leading to substantial residual stress levels in the final components [10,70,71]. In the PBF-LB process, when a new layer is added and heated above the temperature of the underlying part, it initially expands uniformly but is restricted by the cooler underlying material. This results in compressive stresses in the new layer and tensile stresses in the underlying part. During cooling, the new layer contracts faster than the underlying part, resulting in tensile stresses in the new layer and compressive stresses in the underlying part. This heterogeneous solidification process creates residual stresses with the sign of the residual stress typically opposite to the sign of the plastic strain during solidification due to the material strain accommodation between the regions. These stresses are primarily tensile in the new layer and compressive in the underlying material [71]. When stress levels surpass the yield strength of a Ni-base superalloy material, the material tends to release this stress through plastic deformation, leading to distortion of the component's shape or severe cracking, potentially resulting in component failure. Residual stress is identified as the primary factor driving crack initiation. Predictions regarding the likelihood of cracking or distortion during the PBF-LB process must consider the size and shape of the components, as these characteristics are closely linked to residual stress levels [10]. Among the PBF-LB process parameters, the scanning strategy is one of the most important process parameters to control residual stress [10,13,15,21,49,58,70,71].

In our study, Fig. 14 presents the principal residual stress graphs of the samples, showing a notable difference between the XZ and XY planes, highlighting anisotropy between these planes. This aligns with findings by Bartlett and Li [71], who reported that anisotropy in in-plane stresses is significant in additive manufacturing due to the non-uniform melting of layers by discrete beam tracks. Longitudinal stresses along the beam motion direction are generally much higher than transverse stresses because of the non-uniform temperature distribution and contraction during solidification and cooling. Experimental data indicate that longitudinal stresses can be 1.5–2.5 times greater than transverse stresses. This anisotropy is present within each beam track and combines to produce an anisotropic total stress field in each layer. Furthermore, the observed differences in residual stress values among the samples are attributed to the distinct thermal histories and cooling rates associated with each scanning strategy in the PBF-LB process.

The alternating bi-directional scanning strategies, including the 0° and 90° rotation between layers, create linear and consistent heat input paths that generate higher thermal gradients and uneven cooling, resulting in elevated residual stresses. Specifically, the 0° sample exhibited the highest residual stress in both the XZ and XY planes, consistent with previous findings by Zhang et al. [72] and Robinson et al. [73] and was associated with crack formation. Also, the cracks

observed in the XZ plane of the 90° sample (Fig. 4(d)) can be attributed to the high σ_{max} residual stress present in those areas. In contrast, the 45° and 67° samples, which introduce angled thermal gradients, lead to more even heat distribution and smoother temperature gradients, thereby reducing the magnitude of residual stresses compared to the linear scanning methods. The 67° sample exhibited the lowest σ_{max} residual stress in the XZ planes of the samples due to uniform thermal conditions during laser scanning, consistent with Xu et al. [28]. This uniformity helps to distribute the heat more evenly across the build area, reducing the magnitude of thermal gradients and resulting in lower residual stresses. Additionally, the high recrystallization fraction in the XZ plane of the 67° sample may further contribute to the reduction of residual stress.

The island/chessboard scanning strategy, with small island sizes and short scan vectors, helps to reduce temperature gradients and residual stress in additively manufactured parts. Combined with rotated scan strategies, this method effectively mitigates residual stress formation by facilitating better heat dissipation and more uniform cooling [13,70]. Among these, the Q67° sample displayed the lowest maximum residual stress in the XZ plane, due to more uniform thermal conditions and a higher recrystallization fraction. However, the Q90° sample showed unexpectedly high residual stress in the XZ plane. The reason for this can be explained as follows. The measured area for residual stress analysis is crucial for accuracy. The results may be affected if the focus is on overlapping regions rather than inside the islands. This is particularly relevant for intricate scanning patterns like the chessboard strategy. Also, it is important to consider that the collimator diameter directly influences XRD residual stress measurements, particularly for the chessboard scanning strategy. About eight small islands of the chessboard scanning strategy should be within the measured area to accurately observe the residual stress. However, in this study, a 2 mm collimator diameter was used, which does not allow for fitting eight different islands in the measured area. As a result, the measured residual stress in the chessboard scanning strategy can be affected by this limitation.

5. Conclusions

This study comprehensively examined the effects of various scanning strategies, including alternating bi-directional scanning with rotation angles of 0°, 45°, 67°, and 90° between adjacent layers, and alternating chessboard scanning with rotation angles of 67° and 90° between adjacent layers. The investigation focused on the relative density, formation of pores and cracks, surface roughness, microstructure, crystallographic texture, microhardness, and residual stress of IN939 fabricated by the PBF-LB process. Aiming to address the research gap, this study explores how different scanning strategies impact the material properties of IN939 fabricated by the PBF-LB. The main findings from the observed results are summarized as follows.

1) The 45° and 67° samples had the highest relative density at 99.3%, while Q90° had the lowest at 99.05%. The 0° and Q67° samples showed the highest porosity at 0.27% and the largest pore sizes. Defect formation was highest in the XZ plane of the 0° sample with bi-directional scanning and the Q67° sample with chessboard scanning. The alternating bi-directional scanning strategy with 67° rotation is optimal for achieving high relative density and small pore size.
2) Solidification, solid-state, and oxide-induced (Al_2O_3) cracks were observed in the as-built samples. The 0° sample had the most severe cracking, with cracks predominantly propagating along the BD in the XZ plane, especially near the edge, and some extending perpendicular to the BD. The 90° sample also showed long cracks in the XZ plane, particularly at the edge. In contrast, the 45° and 67° samples had fewer cracks.
3) The chessboard scanning strategy resulted in higher Sa and Sz values compared to the alternating bi-directional strategy, attributed to overlapping regions and increased spattering from small islands, regardless of rotation angles. Microhardness values across samples were similar, ranging from 321 ± 14 HV to 356± 7 HV.
4) The XZ planes of the 45°, 67°, 90°, Q67°, and Q90° samples featured arc-shaped melt pools and columnar grains, while the 0° samples had directionally elongated grains and fine irregular grains. Distinct chessboard patterns appeared in the XY planes of the 67°, 90°, and Q90° samples, with the 90° sample being the most pronounced, whereas equiaxed grains were visible in the XY plane of the 45° sample. The 0° sample had the largest area-weighted average grain size in the XZ plane but smaller grains in the XY plane compared to the other samples, showing notable anisotropy between the planes.
5) The 0° and 90° samples exhibited a strong cube texture, with PF intensity values of 9.301 and 6.930, and IPF intensity values of 3.999 and 4.514, respectively. Additionally, the 45°, 67°, and Q90° samples showed both <001>//BD and <101>//BD textures, with the Q90° sample having the highest intensity values (6.243 for PFs and 2.238 for IPFs). Overall, the 0° sample showed the most intense texture due to the alignment of the scan, heat flow, and growth directions, while the texture intensity weakened for the 45° and 67° samples.
6) Alternating bi-directional scanning strategies with 0° and 90° rotation angles created significant thermal gradients and uneven cooling, leading to high residual stresses. The 0° sample exhibited the highest σ_{max} residual stress in both the XZ (738.3 MPa) and XY (581.6 MPa) planes. In contrast, 45° and 67° rotation angles provided more uniform heat distribution and lower residual stresses. Among the alternating bi-directional scanning strategies, the 67° sample achieved the lowest σ_{max} residual stress in both the XZ (542.6 MPa) and XY (443.9 MPa) planes due to better thermal uniformity and enhanced recrystallization. Although the island/chessboard strategy reduced temperature gradients, struggled with accuracy because of limitations with collimator diameter and overlapping regions. Overall, the XY plane of the Q67° sample achieved the lowest σ_{max} residual stress (408.4 MPa).

CRediT authorship contribution statement

Merve Nur Doğu: Conceptualization, Methodology, Investigation, Data curation, Writing – original draft, Writing – review & editing, Visualization, Project administration. **Seren Ozer:** Investigation, Writing – review & editing. **Mustafa Alp Yalçın:** Investigation. **Kemal Davut:** Methodology, Resources, Writing – review & editing. **Muhannad Ahmed Obeidi:** Investigation. **Caner Simsir:** Methodology, Resources, Writing – review & editing. **Hengfeng Gu:** Writing – review & editing, Funding acquisition. **Chong Teng:** Writing – review & editing, Funding acquisition. **Dermot Brabazon:** Validation, Resources, Writing – review & editing, Supervision, Project administration, Funding acquisition.

Declaration of competing interest

The authors declare that they have no known competing financial interests or personal relationships that could have appeared to influence the work reported in this paper.

Acknowledgments

This publication has emanated from research supported by a research grant from Science Foundation Ireland (SFI) under grant number 16/RC/3872 and is co-funded under the European Regional Development Fund. This publication has emanated from research supported by the European Union's Horizon 2020 Research and Innovation Program under grant agreement No. 101138859 (DILAPRO). This

publication has emanated from research supported in part by a grant from SFI and I-Form Advanced Manufacturing Centre under Grant number 21/RC/10295_P2. For the purpose of Open Access, the author has applied a CC BY public copyright licence to any Author Accepted Manuscript version arising from this submission.

The optical microscope images were taken at the Nano Research Facility in Dublin City University which was funded under the Programme for Research in Third Level Institutions (PRTLI) Cycle 5. The PRTLI is co-funded through the European Regional Development Fund (ERDF), part of the European Union Structural Funds Programme 2011–2015.

The authors are grateful for EBSD characterizations support from the Metal Forming Center of Excellence at Atilim University.

The authors also thank Middle East Technical University for the residual stress measurements.

Appendix B

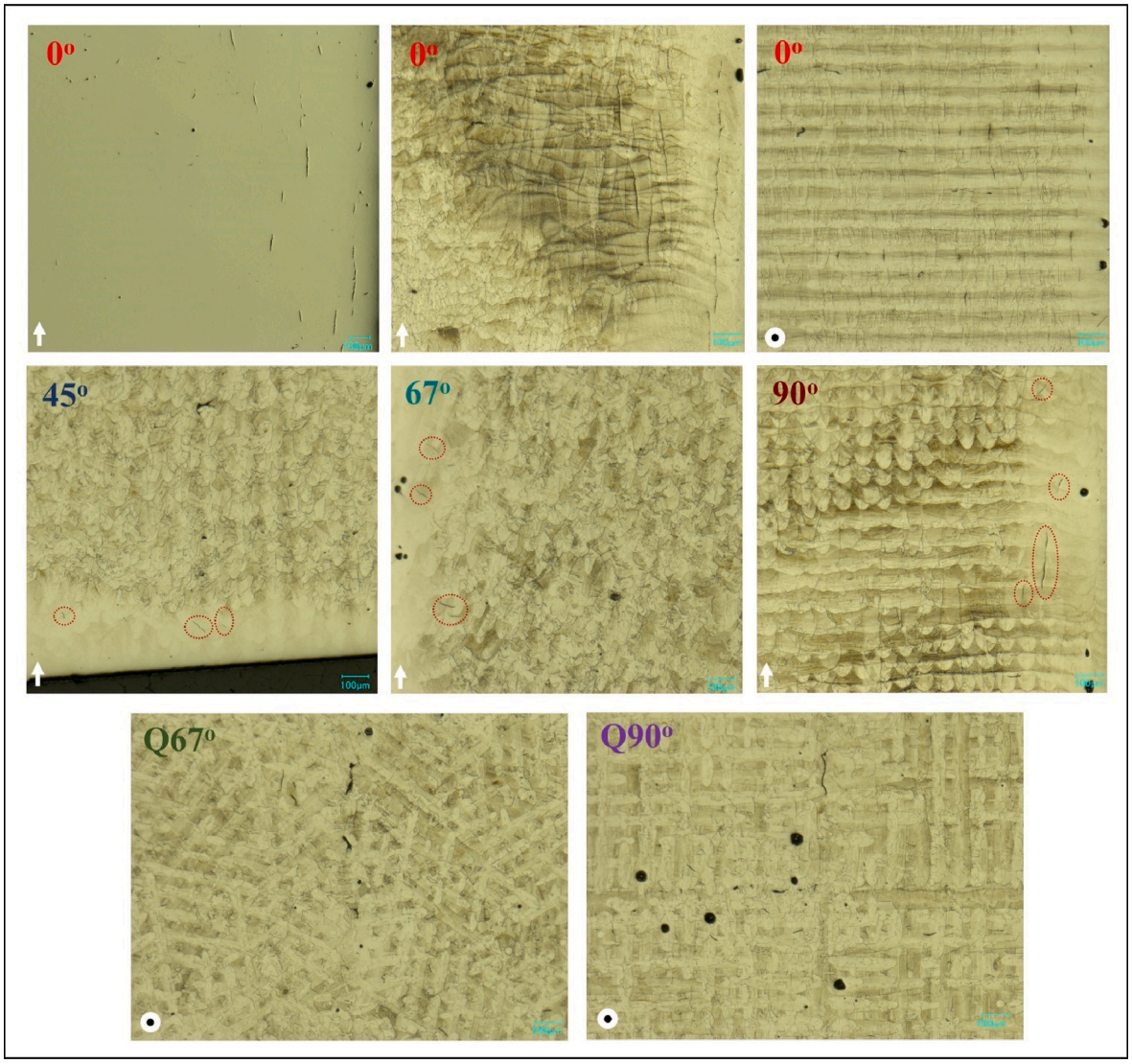

Fig. B1. Optical micrographs of the crack distribution in the XY and XZ planes of the as-built samples: (a) 0°, (b) 45°, (c) 67°, (d) 90°, (e) Q67°, and (f) Q90°.

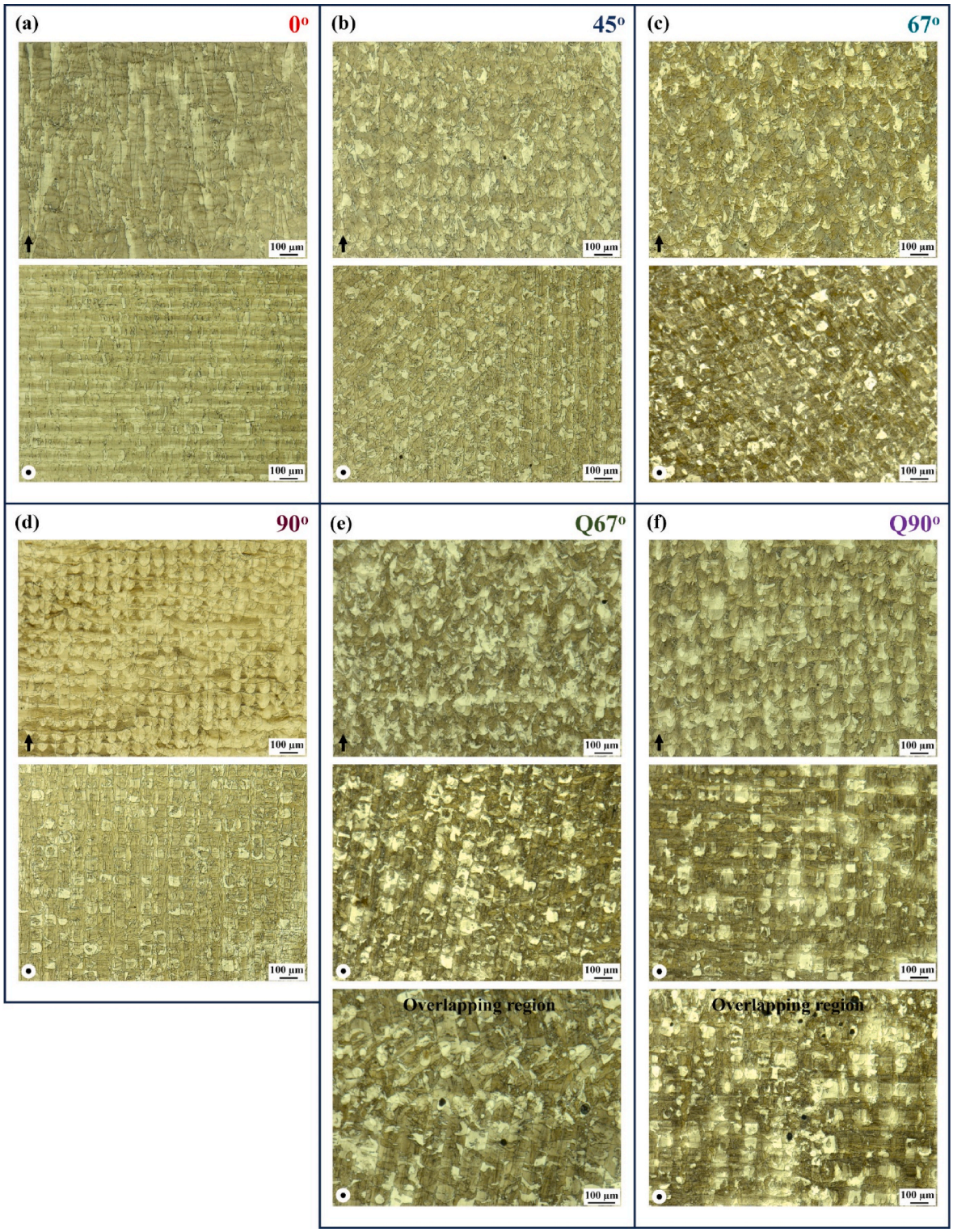

Fig. B2. Optical micrographs of the as-built samples: (a) 0°, (b) 45°, (c) 67°, (d) 90°, (e) Q67°, and (f) Q90°.

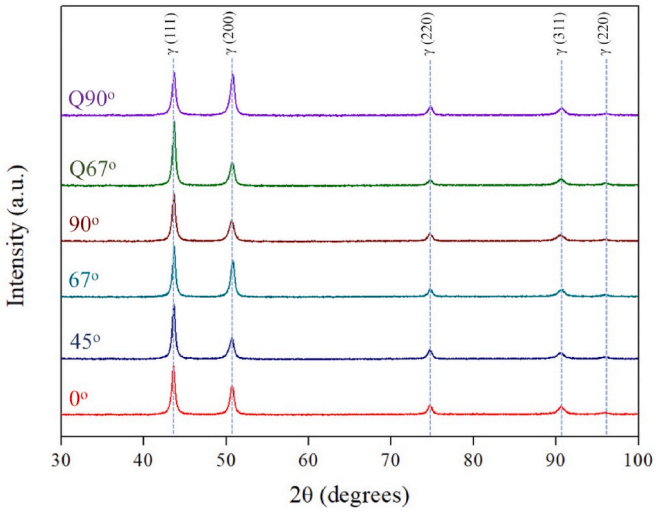

Fig. B3. XRD pattern of the as-built samples.

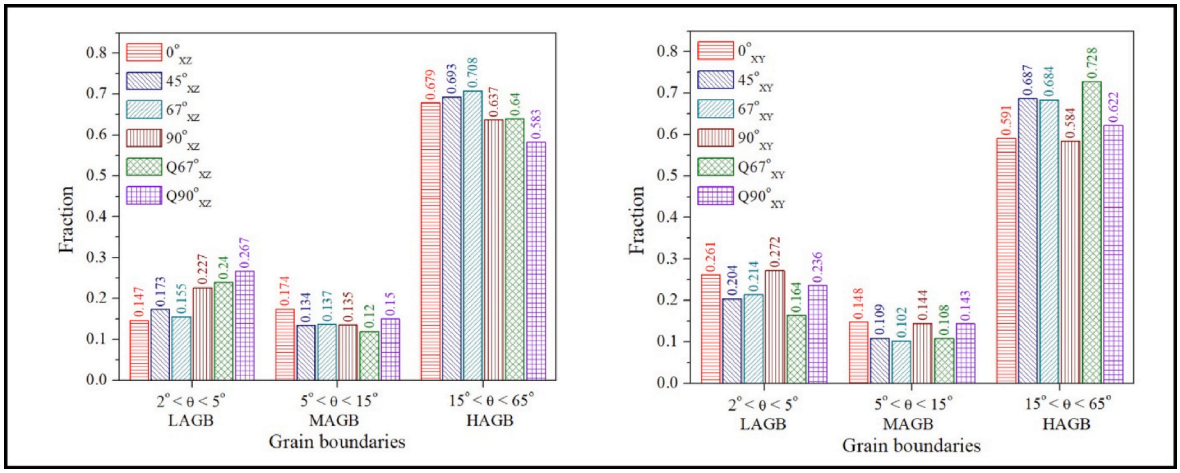

Fig. B4. Grain boundary character distributions for both the XZ and XY planes of the as-built samples.

Here, low-angle grain boundaries (LAGBs) refer to the misorientation angle between 2° and 5°, medium angle grain boundaries (MAGBs) refer to the misorientation angle between 5° and 15°, and high-angle grain boundaries (HAGBs) correspond to grain boundaries with a misorientation angle higher than 15°. According to the literature, HAGBs, which act as repulsive boundaries, are more susceptible to cracking due to their high misorientation and associated energy. They are more readily wetted by liquid films at lower temperatures compared to LAGBs. This results in a wider temperature range for liquid film presence when the misorientation angle is higher. Consequently, HAGBs are more prone to hot cracks, exhibiting greater sensitivity to hot cracking than LAGBs [28,51,59].

References

[1] Doğu MN, Mussatto A, Yalçın MA, Ozer S, Davut K, Obeidi MA, Kumar A, Hudson S, O'Neill D, O'Connor R, Gu H, Brabazon D. A comprehensive characterization of the effect of spatter powder on IN939 parts fabricated by laser powder bed fusion. Mater Des 2023;235. https://doi.org/10.1016/j.matdes.2023.112406.

[2] Chlebus E, Gruber K, Kuźnicka B, Kurzac J, Kurzynowski T. Effect of heat treatment on the microstructure and mechanical properties of Inconel 718 processed by selective laser melting. Mater Sci Eng, A 2015;639:647–55. https://doi.org/10.1016/j.msea.2015.05.035.

[3] Gordon JV, Narra SP, Cunningham RW, Liu H, Chen H, Suter RM, Beuth JL, Rollett AD. Defect structure process maps for laser powder bed fusion additive manufacturing. Addit Manuf 2020;36. https://doi.org/10.1016/j.addma.2020.101552.

[4] Dogu MN, McCarthy E, McCann R, Mahato V, Caputo A, Bambach M, Ahad IU, Brabazon D. Digitisation of metal AM for part microstructure and property control. Int J Material Form 2022;15. https://doi.org/10.1007/s12289-022-01686-4.

[5] Doğu MN, Davut K, Obeidi MA, Yalçın MA, Gu H, Low TSE, Ginn J, Brabazon D. Recrystallization and grain growth kinetics of IN718 manufactured by laser powder bed fusion. J Mater Res Technol 2022;19:4242–57. https://doi.org/10.1016/j.jmrt.2022.06.157.

[6] Obeidi MA. Metal additive manufacturing by laser-powder bed fusion:Guidelines for process optimisation. Results in Engineering 2022;15:100473. https://doi.org/10.1016/j.rineng.2022.100473.

[7] Du C, Zhao Y, Jiang J, Wang Q, Wang H, Li N, Sun J. Pore defects in laser powder bed fusion: formation mechanism, control method, and perspectives. J Alloys Compd 2023;944. https://doi.org/10.1016/j.jallcom.2023.169215.

[8] Wang J, Zhu R, Liu Y, Zhang L. Understanding melt pool characteristics in laser powder bed fusion: an overview of single- and multi-track melt pools for process optimization. Advanced Powder Materials 2023;2. https://doi.org/10.1016/j.apmate.2023.100137.

[9] Qi X, Liang X, Wang J, Zhang H, Wang X, Liu Z. Microstructure tailoring in laser powder bed fusion (L-PBF): strategies, challenges, and future outlooks. J Alloys Compd 2024;970. https://doi.org/10.1016/j.jallcom.2023.172564.

[10] Guo C, Li G, Li S, Hu X, Lu H, Li X, Xu Z, Chen Y, Li Q, Lu J, Zhu Q. Additive manufacturing of Ni-based superalloys: residual stress, mechanisms of crack formation and strategies for crack inhibition. Nano Materials Science 2023;5:53–77. https://doi.org/10.1016/j.nanoms.2022.08.001.

[11] Oliveira JP, LaLonde AD, Ma J. Processing parameters in laser powder bed fusion metal additive manufacturing. Mater Des 2020;193:1–12. https://doi.org/10.1016/j.matdes.2020.108762.

[12] Liu L, Wang D, Yang Y, Wang Z, Qian Z, Wu S, Tang J, Han C, Tan C. Effect of scanning strategies on the microstructure and mechanical properties of inconel 718

alloy fabricated by laser powder bed fusion. Adv Eng Mater 2023;25. https://doi.org/10.1002/adem.202200492.
[13] Jia H, Sun H, Wang H, Wu Y, Wang H. Scanning strategy in selective laser melting (SLM): a review. Int J Adv Manuf Technol 2021;113:2413–35. https://doi.org/10.1007/s00170-021-06810-3.
[14] Mussatto A, Groarke R, Vijayaraghavan RK, Obeidi MA, McNally PJ, Nicolosi V, Delaure Y, Brabazon D. Laser-powder bed fusion of silicon carbide reinforced 316L stainless steel using a sinusoidal laser scanning strategy. J Mater Res Technol 2022;18:2672–98. https://doi.org/10.1016/j.jmrt.2022.03.170.
[15] Serrano-Munoz I, Ulbricht A, Fritsch T, Mishurova T, Kromm A, Hofmann M, Wimpory RC, Evans A, Bruno G. Scanning manufacturing parameters determining the residual stress state in LPBF IN718 small parts. Adv Eng Mater 2021;23. https://doi.org/10.1002/adem.202100158.
[16] Pant P, Salvemini F, Proper S, Luzin V, Simonsson K, Sjöström S, Hosseini S, Peng RL, Moverare J. A study of the influence of novel scan strategies on residual stress and microstructure of L-shaped LPBF IN718 samples. Mater Des 2022;214. https://doi.org/10.1016/j.matdes.2022.110386.
[17] Paraschiv A, Matache G, Constantin N, Vladut M. Investigation of scanning strategies and laser remelting effects on top surface deformation of additively manufactured in 625. Materials 2022;15. https://doi.org/10.3390/ma15093198.
[18] Dunbar AJ, Denlinger ER, Heigel J, Michaleris P, Guerrier P, Martukanitz R, Simpson TW. Development of experimental method for in situ distortion and temperature measurements during the laser powder bed fusion additive manufacturing process. Addit Manuf 2016;12:25–30. https://doi.org/10.1016/j.addma.2016.04.007.
[19] Paraschiv A, Matache G, Vladut M. Assessment of residual stresses in laser powder bed fusion manufactured in 625. Materials 2024;17. https://doi.org/10.3390/ma17020413.
[20] Arısoy YM, Criales LE, Özel T, Lane B, Moylan S, Donmez A. Influence of scan strategy and process parameters on microstructure and its optimization in additively manufactured nickel alloy 625 via laser powder bed fusion. Int J Adv Manuf Technol 2017;90:1393–417. https://doi.org/10.1007/s00170-016-9429-z.
[21] Nadammal N, Mishurova T, Fritsch T, Serrano-Munoz I, Kromm A, Haberland C, Portella PD, Bruno G. Critical role of scan strategies on the development of microstructure, texture, and residual stresses during laser powder bed fusion additive manufacturing. Addit Manuf 2021;38. https://doi.org/10.1016/j.addma.2020.101792.
[22] Diepold B, Palm MS, Wimmer A, Sebald T, Höppel HW, Neumeier S, Göken M. Rotating scan strategy induced anisotropic microstructural and mechanical behavior of selective laser melted materials and their reduction by heat treatments. Adv Eng Mater 2021;23. https://doi.org/10.1002/adem.202100622.
[23] Gokcekaya O, Ishimoto T, Hibino S, Yasutomi J, Narushima T, Nakano T. Unique crystallographic texture formation in Inconel 718 by laser powder bed fusion and its effect on mechanical anisotropy. Acta Mater 2021;212:116876. https://doi.org/10.1016/j.actamat.2021.116876.
[24] Wan HY, Zhou ZJ, Li CP, Chen GF, Zhang GP. Effect of scanning strategy on grain structure and crystallographic texture of Inconel 718 processed by selective laser melting. J Mater Sci Technol 2018;34:1799–804. https://doi.org/10.1016/j.jmst.2018.02.002.
[25] Dai K, He X, Zhang W, Kong D, Guo R, Hu M, He K, Dong C. Tailoring the microstructure and mechanical properties for Hastelloy X alloy by laser powder bed fusion via scanning strategy. Mater Des 2023;235. https://doi.org/10.1016/j.matdes.2023.112386.
[26] Zhang X, Xu H, Li Z, Dong A, Du D, Lei L, Zhang G, Wang D, Zhu G, Sun B. Effect of the scanning strategy on microstructure and mechanical anisotropy of Hastelloy X superalloy produced by Laser Powder Bed Fusion. Mater Char 2021;173. https://doi.org/10.1016/j.matchar.2021.110951.
[27] Carter LN, Martin C, Withers PJ, Attallah MM. The influence of the laser scan strategy on grain structure and cracking behaviour in SLM powder-bed fabricated nickel superalloy. J Alloys Compd 2014;615:338–47. https://doi.org/10.1016/j.jallcom.2014.06.172.
[28] Xu J, Ding Y, Gao Y, Wang H, Hu Y, Zhang D. Grain refinement and crack inhibition of hard-to-weld Inconel 738 alloy by altering the scanning strategy during selective laser melting. Mater Des 2021;209:109940. https://doi.org/10.1016/j.matdes.2021.109940.
[29] Doğu MN, Ozer S, Yalçın MA, Davut K, Bilgin GM, Obeidi MA, Brodin H, Gu H, Brabazon D. Effect of solution heat treatment on the microstructure and crystallographic texture of IN939 fabricated by powder bed fusion-laser beam. J Mater Res Technol 2023;24. https://doi.org/10.1016/j.jmrt.2023.05.152.
[30] Rakoczy Ł, Grudzień-Rakoczy M, Rutkowski B, Cygan R, Zielińska-Lipiec A. The role of the microstructural changes during induction preheating on the HAZ liquation cracking susceptibility of Ni-based superalloy. J Mater Sci 2024;59:631–49. https://doi.org/10.1007/s10853-023-09184-x.
[31] Kazempour-Liasi H, Tajally M, Abdollah-Pour H. Liquation cracking in the heat-affected zone of IN939 superalloy tungsten inert gas weldments. Int J Miner Metall Mater 2020;27:764–73. https://doi.org/10.1007/s12613-019-1954-y.
[32] Kazempour-Liasi H, Tajally M, Abdollah-Pour H. Effects of pre- and post-weld heat treatment cycles on the liquation and strain-age cracking of IN939 superalloy. Engineering Research Express 2019;1. https://doi.org/10.1088/2631-8695/ab4d6c.
[33] Tang YT, Panwisawas C, Ghoussoub JN, Gong Y, Clark JWG, Németh AAN, McCartney DG, Reed RC. Alloys-by-design: application to new superalloys for additive manufacturing. Acta Mater 2021;202:417–36. https://doi.org/10.1016/j.actamat.2020.09.023.
[34] Zhang B, Ding H, Meng AC, Nemati S, Guo S, Meng WJ. Crack reduction in Inconel 939 with Si addition processed by laser powder bed fusion additive manufacturing. Addit Manuf 2023;72. https://doi.org/10.1016/j.addma.2023.103623.
[35] Ozer S, Doğu MN, Ozdemirel C, Bilgin GM, Gunes M, Davut K, Gu H, Brabazon D. Effect of aging treatment on the microstructure, cracking type and crystallographic texture of IN939 fabricated by powder bed fusion-laser beam. J Mater Res Technol 2024;33:574–88. https://doi.org/10.1016/j.jmrt.2024.09.106.
[36] Marchese G, Parizia S, Saboori A, Manfredi D, Lombardi M, Fino P, Ugues D, Biamino S. The influence of the process parameters on the densification and microstructure development of laser powder bed fused inconel 939. Metals 2020;10:1–19. https://doi.org/10.3390/met10070882.
[37] Šulák I, Babinský T, Chlupová A, Milovanović A, Náhlík L. Effect of building direction and heat treatment on mechanical properties of Inconel 939 prepared by additive manufacturing. J Mech Sci Technol 2023;37:1071–6. https://doi.org/10.1007/s12206-022-2101-7.
[38] Dursun G, Orhangul A, Urkmez A, Akbulut G. Understanding the parameter effects on densification and single track formation of laser powder bed fusion inconel 939. In: Procedia CIRP. Elsevier B.V.; 2022. p. 258–63. https://doi.org/10.1016/j.procir.2022.03.045.
[39] Volpato GM, Tetzlaff U, Fredel MC. A comprehensive literature review on laser powder bed fusion of Inconel superalloys. Addit Manuf 2022;55. https://doi.org/10.1016/j.addma.2022.102871.
[40] Kanagarajah P, Brenne F, Niendorf T, Maier HJ. Inconel 939 processed by selective laser melting: effect of microstructure and temperature on the mechanical properties under static and cyclic loading. Mater Sci Eng 2013;588:188–95. https://doi.org/10.1016/j.msea.2013.09.025.
[41] Rodríguez-Barber I, Fernández-Blanco AM, Unanue-Arruti I, Madariaga-Rodríguez I, Milenkovic S, Pérez-Prado MT. Laser powder bed fusion of the Ni superalloy Inconel 939 using pulsed wave emission. Mater Sci Eng, A 2023;870. https://doi.org/10.1016/j.msea.2023.144864.
[42] Fardan A, Klement U, Brodin H, Hryha E. Effect of Part Thickness and build angle on the microstructure, surface roughness, and mechanical properties of additively manufactured IN-939. Metall Mater Trans A Phys Metall Mater Sci 2023;54:1792–807. https://doi.org/10.1007/s11661-022-06940-7.
[43] Shaikh AS. Development of a γ' precipitation hardening Ni-base superalloy for additive manufacturing. 2018. p. 102. Thesis.
[44] Doğu MN, Obeidi MA, Gu H, Teng C, Brabazon D. Powder bed fusion–laser beam of IN939: the effect of process parameters on the relative density, defect formation, surface roughness and microstructure. Materials 2024;17. https://doi.org/10.3390/ma17133324.
[45] Bunge H-J. Texture analysis in materials science. https://doi.org/10.1016/B978-0-408-10642-9.50006-4; 1982.
[46] ASTM B311-17, Standard Test Method for Density of Powder Metallurgy (PM) Materials Containing Less Than Two Percent Porosity, (n.d.). https://doi.org/10.1520/B0311-17.
[47] EOS. Nickel alloy IN939 material data sheet metal solutions. https://www.eos.info/en-us/metal-solutions/metal-materials/data-sheets/mds-eos-nickelalloy-in939; 2020.
[48] ASTM International. Standard Test Method for Microindentation Hardness of Materials - ASTM E384 - 17 2017.
[49] Çelik G. The influence of additive manufacturing process parameters on residual stress of 17-4 PH stainless Steel parts manufactured by laser powder bed fusion additive manufacturing system. M.Sc. Thesis; 2023.
[50] ASTM International, E915-Standard Test Method for Verifying the Alignment of X-Ray Diffraction Instrumentation for Residual Stress Measurement, (n.d.). https://doi.org/10.1520/E0915-19.
[51] Wei Q, Xie Y, Teng Q, Shen M, Sun S, Cai C. Crack types, mechanisms, and suppression methods during high-energy beam additive manufacturing of nickel-based superalloys: a review. Chin J Mech Eng: Additive Manufacturing Frontiers 2022;1:100055. https://doi.org/10.1016/j.cjmeam.2022.100055.
[52] Hafezi M, Kermanpur A, Rezaeian A, Saeidirad S, Nikneshan V, Rabieifar H, Kamouri Yousefabad E. Investigating crack formation in IN738LC Ni-based superalloy fabricated by laser powder-bed fusion process. J Mater Res Technol 2024;29:1983–2002. https://doi.org/10.1016/j.jmrt.2024.01.264.
[53] Aota LS, Bajaj P, Zilnyk KD, Jägle EA, Ponge D, Sandim HRZ, Raabe D. Recrystallization kinetics, mechanisms, and topology in alloys processed by laser powder-bed fusion: AISI 316L stainless steel as example. Materialia (Oxf) 2021;20:101236. https://doi.org/10.1016/j.mtla.2021.101236.
[54] Pinto FC, Aota LS, Souza Filho IR, Raabe D, Sandim HRZ. Recrystallization in non-conventional microstructures of 316L stainless steel produced via laser powder-bed fusion: effect of particle coarsening kinetics. J Mater Sci 2022;57:9576–98. https://doi.org/10.1007/s10853-021-06859-1.
[55] de Sonis E, Dépinoy S, Giroux PF, Maskrot H, Lemarquis L, Hercher O, Villaret F, Gourgues-Lorenzon AF. Dependency of recrystallization kinetics on the solidification microstructure of 316L stainless steel processed by laser powder bed fusion (LPBF). Mater Char 2022;194. https://doi.org/10.1016/j.matchar.2022.112370.
[56] Buerstmayr R, Theska F, Kozeschnik E, Webster RF, Lison-Pick M, Street S, Primig S. Investigation and simulation of the effects of nm-scale γ' precipitates on the recrystallization of Ni-based superalloys. Metall Mater Trans A Phys Metall Mater Sci 2023;54:2259–76. https://doi.org/10.1007/s11661-023-07008-w.
[57] Lu Y, Wu S, Gan Y, Huang T, Yang C, Junjie L, Lin J. Study on the microstructure, mechanical property and residual stress of SLM Inconel-718 alloy manufactured by differing island scanning strategy. Opt Laser Technol 2015;75:197–206. https://doi.org/10.1016/j.optlastec.2015.07.009.

[58] Ali H, Ghadbeigi H, Mumtaz K. Effect of scanning strategies on residual stress and mechanical properties of Selective Laser Melted Ti6Al4V. Mater Sci Eng, A 2018; 712:175–87. https://doi.org/10.1016/j.msea.2017.11.103.
[59] Griffiths S, Ghasemi Tabasi H, Ivas T, Maeder X, De Luca A, Zweiacker K, Wróbel R, Jhabvala J, Logé RE, Leinenbach C. Combining alloy and process modification for micro-crack mitigation in an additively manufactured Ni-base superalloy. Addit Manuf 2020;36. https://doi.org/10.1016/j.addma.2020.101443.
[60] Mukherjee T, Elmer JW, Wei HL, Lienert TJ, Zhang W, Kou S, DebRoy T. Control of grain structure, phases, and defects in additive manufacturing of high-performance metallic components. Prog Mater Sci 2023;138. https://doi.org/10.1016/j.pmatsci.2023.101153.
[61] Cobbinah PV, Matsunaga S, Yamabe-Mitarai Y. Controlled crystallographic texture orientation in structural materials using the laser powder bed fusion process—a review. Adv Eng Mater 2023;25. https://doi.org/10.1002/adem.202300819.
[62] Song Y, Sun Q, Guo K, Wang X, Liu J, Sun J. Effect of scanning strategies on the microstructure and mechanical behavior of 316L stainless steel fabricated by selective laser melting. Mater Sci Eng, A 2020;793. https://doi.org/10.1016/j.msea.2020.139879.
[63] Kouraytem N, Varga J, Amin-Ahmadi B, Mirmohammad H, Chanut RA, Spear AD, Kingstedt OT. A recrystallization heat-treatment to reduce deformation anisotropy of additively manufactured Inconel 718. Mater Des 2021;198. https://doi.org/10.1016/j.matdes.2020.109228.
[64] Huang K, Logé RE. A review of dynamic recrystallization phenomena in metallic materials. Mater Des 2016;111:548–74. https://doi.org/10.1016/j.matdes.2016.09.012.
[65] Sabzi HE, Li XH, Zhang C, Fu H, San-Martín D, Rivera-Díaz-del-Castillo PEJ. Deformation twinning-induced dynamic recrystallization during laser powder bed fusion. Scripta Mater 2022;207. https://doi.org/10.1016/j.scriptamat.2021.114307.
[66] Sabzi HE, Aboulkhair NT, Liang X, Li XH, Simonelli M, Fu H, Rivera-Díaz-del-Castillo PEJ. Grain refinement in laser powder bed fusion: the influence of dynamic recrystallization and recovery. Mater Des 2020;196. https://doi.org/10.1016/j.matdes.2020.109181.
[67] DebRoy T, Wei HL, Zuback JS, Mukherjee T, Elmer JW, Milewski JO, Beese AM, Wilson-Heid A, De A, Zhang W. Additive manufacturing of metallic components – process, structure and properties. Prog Mater Sci 2018;92:112–224. https://doi.org/10.1016/j.pmatsci.2017.10.001.
[68] Zhao J, Sun L, Ji P, Yu X, Chen L, Liu S, Zheng K, Yin F. The effect of scanning strategies on the microstructure and mechanical properties of M2052 alloy manufactured by selective laser melting. J Mater Res Technol 2023;27:7084–93. https://doi.org/10.1016/j.jmrt.2023.11.141.
[69] Hariharan VS, Kaushik R, Murty BS, Phanikumar G. Effect of laser scan rotation on the microstructure and mechanical properties of laser powder bed fused Haynes 282. Materialia (Oxf) 2024;33. https://doi.org/10.1016/j.mtla.2023.101992.
[70] Kumar VP, Jebaraj AV. Comprehensive review on residual stress control strategies in laser-based powder bed fusion process– Challenges and opportunities. Lasers in Manufacturing and Materials Processing 2023;10:400–42. https://doi.org/10.1007/s40516-023-00217-6.
[71] Bartlett JL, Li X. An overview of residual stresses in metal powder bed fusion. Addit Manuf 2019;27:131–49. https://doi.org/10.1016/j.addma.2019.02.020.
[72] Zhang W, Guo D, Wang L, Davies CM, Mirihanage W, Tong M, Harrison NM. X-ray diffraction measurements and computational prediction of residual stress mitigation scanning strategies in powder bed fusion additive manufacturing. Addit Manuf 2023;61. https://doi.org/10.1016/j.addma.2022.103275.
[73] Robinson J, Ashton I, Fox P, Jones E, Sutcliffe C. Determination of the effect of scan strategy on residual stress in laser powder bed fusion additive manufacturing. Addit Manuf 2018;23:13–24. https://doi.org/10.1016/j.addma.2018.07.001.